Fermi National Accelerator Laboratory

FERMILAB-Pub-89/69-E
[E-605]

High Transverse Momentum Single Hadron Production in *pp* and *pd* Collisions at $\sqrt{s}$ = 27.4 and $\sqrt{s}$ = 38.8 GeV*

D. E. Jaffe[8,a], P. B. Straub[9], M. R. Adams[8,a], C. N. Brown[4], G. Charpak[2], W. E. Cooper[4], J. A. Crittenden[3,b], D. A. Finley[4], H. D. Glass[8,c], R. Gray[9,d], Y. Hemmi[7], Y. B. Hsiung[3,e], J. R. Hubbard[1], A. M. Jonckheere[4], H. Jöstlein[4], D. M. Kaplan[5,f], L. M. Lederman[4], K. B. Luk[9,e], A. Maki[6], Ph. Mangeot[1], R. L. McCarthy[8], K. Miyake[7], R. E. Plaag[9,g], J. P. Rutherfoord[9,h], Y. Sakai[6], J. C. Santiard[2], F. Sauli[2], S. R. Smith[3], T. Yoshida[7], and K. K. Young[9]

1) CEN Saclay, Gif-sur-Yvette, 91190 France
2) CERN, CH-1124 Geneva, 23 Switzerland
3) Columbia University, New York, New York 10027
4) Fermi National Accelerator Laboratory, Batavia, Illinois 60510
5) Florida State University, Tallahassee, Florida 32306
6) KEK, Tsukuba, Ibaraki-ken, 305 Japan
7) Kyoto University, Kyoto, 606 Japan
8) State University of New York, Stony Brook, New York 11794
9) University of Washington, Seattle, Washington 98195

March 21, 1989

* Submitted to Phys. Rev. D

HIGH TRANSVERSE MOMENTUM SINGLE HADRON PRODUCTION IN *pp* AND *pd* COLLISIONS AT $\sqrt{s} = 27.4$ AND $\sqrt{s} = 38.8$ *GeV*

21 March 1989

D.E. Jaffe,[8a] P.B. Straub,[9] M.R. Adams,[8a] C.N. Brown,[4] G. Charpak,[2] W.E. Cooper,[4] J.A. Crittenden,[3b] D.A. Finley,[4] H.D. Glass,[8c] R. Gray,[9d] Y. Hemmi,[7] Y.B. Hsiung,[3e] J.R. Hubbard,[1] A.M. Jonckheere,[4] H. Jöstlein,[4] D.M. Kaplan,[5f] L.M. Lederman,[4] K.B. Luk,[9e] A. Maki,[6] Ph. Mangeot,[1] R.L. McCarthy,[8] K. Miyake,[7] R.E. Plaag,[9g] J.P. Rutherfoord,[9h] Y. Sakai,[6] J.C. Santiard,[2] F. Sauli,[2] S.R. Smith,[3] T. Yoshida,[7] and K.K. Young[9]

1) CEN Saclay, Gif-sur-Yvette, 91190 France
2) CERN, CH-1124 Geneva, 23 Switzerland
3) Columbia University, New York, New York 10027
4) FNAL, Batavia, Illinois 60510
5) Florida State University, Tallahassee, Florida 32306
6) KEK, Tsukuba, Ibaraki-ken, 305 Japan
7) Kyoto University, Kyoto, 606 Japan
8) State University of New York, Stony Brook, New York 11794
9) University of Washington, Seattle, Washington 98195

a) Present address: University of Illinois at Chicago, Chicago, Illinois 60680
b) Present address: Physikalisches Institut der Universität Bonn, Nußallee 12, 5300 Bonn 1, Federal Republic of Germany
c) Present address: Aerospace Corporation, El Segundo, California 90245
d) Present address: Falkiner High Energy Physics Department, School of Physics, University of Sydney, Sydney, New South Wales 2006, Australia
e) Present address: FNAL, Batavia, Illinois 60510
f) Present address: Northern Illinois University, Dekalb, Illinois 60115
g) Present address: High Technology Center, Boeing Electronics Co., P.O. Box 24969, MS7J-56, Seattle, Washington 98124-6269
h) Present address: University of Arizona, Tucson, Arizona 85721

Abstract

Results of high transverse momentum charged hadron production in 400 *GeV/c* proton-proton and proton-deuteron collisions and 800 *GeV/c* proton-proton collisions are presented. The transverse momentum range of the data is from 5.2 to 9.0 *GeV/c* for the 400 *GeV/c* collisions and from 3.6 to 11.0 *GeV/c* for the 800 *GeV/c* collisions; the data are centered around 90° in the proton-nucleon center-of-momentum system. Single pion invariant cross sections and particle ratios were measured at both energies. The results are compared to previous experiments and the Lund model.

I. Introduction

Since the first observations at the ISR, large transverse momentum(p_T) hadrons produced in proton–nucleon collisions have been a fruitful source of data on the parton constituents of hadrons. They have also been shown[1] to carry substantial fractions of the momenta of their parent constituents. Thus the study of high p_T pion production can elucidate the interaction mechanism of the constituents of the nucleon. To this end, high p_T charged pion production has been investigated at Fermilab[2] and the CERN intersecting storage rings.[3]

In addition the quantum numbers of high p_T hadrons have been shown to be correlated with the flavor of the scattered parton.[1,4,5] The measurement of the relative production rates of charged pions, kaons and protons provides insight into the structure of the nucleon and the subsequent fragmentation of the struck partons. The measurements of this experiment are compared with the Lund monte carlo predictions for high p_T hadron production[6] which has successfully modelled inclusive meson and baryon production in electron–positron interactions.[7]

This article presents results of charged hadron production near 90° in the proton–nucleon center-of-momentum system(CMS) in pp collisions at $\sqrt{s} = 27.4$ and 38.8 GeV and pd collisions at $\sqrt{s} = 27.4$ GeV taken between January and July of 1984 in the Meson East beamline at Fermilab. Table 1 displays the range in p_T , $x_T = 2p_T/\sqrt{s}$ and CMS production angle(Θ^*) examined.

II. Apparatus and Data Analysis

II.A. Overview

Experiment 605 (E605) at Fermilab[8,9,10] was based upon a focusing magnetic spectrometer designed to study long-lived, charged, high p_T particles near 90° in the proton-nucleon center-of-momentum system produced in 400 and 800 GeV/c proton-nucleus collisions. See Figure 1. Tracking information was provided by six planes of multiwire proportional chambers at station 1 and six planes of drift chambers at station 2 and station 3. Charged pions, kaons and protons were identified with a ring-imaging Cherenkov counter. Electrons were differentiated from hadrons by calorimetry, and muons were identified by scintillation counter hodoscopes and proportional tubes behind more than twenty absorption lengths of dense shielding.

An important modification to the E605 spectrometer, described in detail in reference 9, was the repositioning of the target upstream to accommodate an additional spectrometer magnet(SM0) and a low-angle, tungsten collimator. In addition a series of lead/tungsten baffles were installed in the large SM12 magnet as shown in Figure 2. For these data, SM0, SM12 and SM3 had transverse momentum kicks of approximately 1.3, 7.5 and 0.9 (0., 7.5 and -0.9)GeV/c , respectively, for the 400(800) GeV/c data. These modifications increased the high p_T acceptance and reduced the backgrounds in the rest of the apparatus.

II. B. Beam and Target

A 400 or 800 *GeV/c* proton beam struck a cylindrical target vessel with 25 micron stainless steel walls, 5.08 centimeters in diameter and 20.2 centimeters along the beam filled with either liquid hydrogen(LH_2) or deuterium(LD_2). The beam profile at the target was determined to be roughly gaussian in both the vertical(Y) and horizontal(X) directions with a vertical root-mean-square(RMS) width of .19 mm and a horizontal RMS width of about 2.3 mm.[11] The magnetic field of the spectrometer magnets was in the X-direction so that charged particles were bent vertically. The LH_2 used in the target was measured[12] to be $> 99.99\%$ pure; the two different batches of liquid deuterium used were found to be 98.5% D_2, 1.5% HD and 95% D_2, 5% HD (percent by volume), respectively. No correction was applied to the measurement of the single pion cross section to account for the slight hydrogen contamination of the "deuterium" target resulting in a systematic uncertainty in the *pd* cross section of $\pm 2.0\%$ [limit of error]. To correct the cross section for secondary particle production in the target vessel, one empty target run was taken for about every 3(4) $LH_2(LD_2)$ data runs. The correction applied was less than 2% for all values of p_T .

The beam intensity was monitored by a secondary emission monitor (SEM) calibrated by foil activation once during each of the 400 and 800 *GeV/c* running periods. The results of the calibration were $(8.14 \pm .31) \times 10^7$and $(8.52 \pm .53) \times 10^7$ protons-on-target per SEM count for the 400 and 800 *GeV/c* running periods, respectively. Table 2 lists the total integrated luminosity for each data set. In addition, a four counter telescope pointed at the target perpendicular to the incident beam monitored the interaction rate in the target.

II. C. Hadron Species Identification

Hadron identification was achieved using a large aperture ring-imaging Cherenkov detector.[10,13,14] Photons emitted in a 15.2 m long radiator of ultra-pure helium reflected off a 4×4 array of mirrors onto two multistep proportional wire chambers. The ring radius for the highest momentum track was 70 mm. The ring radius resolution is about 1 mm, primarily due to the chromatic dispersion of the helium. Using samples of high momentum muons, several detector parameters were tabulated for each run. These include the index of refraction and chromatic dispersion of the helium, the number distributions of reconstructed signal and noise photons for each track and the orientation of the mirrors. For each hadron track, this information was used to calculate the likelihood for the reconstructed photon pattern to be produced under each of the three hadron hypotheses. For a track with n photons, the likelihood was a probability density over the n photon positions. A typical high momentum pion had 2.2 reconstructed photons on the ring. There were typically 1.6 noise photons reconstructed within 85 mm of the ring center. Thus for each track, the likelihoods, L_i^α, were computed (greek indices run over π, $K$and p, and i is the track index). For an ensemble of N tracks in a given kinematic bin, the hadron fractions f_π, f_K and f_p ($\sum_\alpha f_\alpha = 1$) were determined by solving the likelihood equations

$$f_\alpha = \sum_{i=1}^{N} \frac{L_i^\alpha f_\alpha}{\sum_\beta L_i^\beta f_\beta}.$$

II. D. Triggering

The single hadron trigger employed two elements – a high-speed, hardware look-up table (the "trigger matrix") and a calorimeter energy signal – described in an earlier article.[9]

For these data, the trigger matrices contained the combinations of hodoscope counters in stations 1, 2 and 3 corresponding to a particle trajectory from the target through the upper ("YU") and lower("YD") aperture of the SM12 magnet. The logical OR of these two signals formed the "Y" trigger element.

Two calorimeter total energy signals were formed: 1) a high-threshold signal, dubbed "EHI", and 2) a lower threshold signal, dubbed "ETFI". In addition energy sums corresponding to localized deposits in the upper ("EU") or lower ("ED") portion of the calorimeter were formed and combined with "YU" and "YD", respectively, to form a trigger designed to accept single high p_T hadrons.

For the 400 GeV/c data, the EU·YU and ED·YD triggers were used in combination with ETFI, pre-scaled to an acceptable rate, and EHI. In the 800 GeV/c run, the EHI·Y trigger was substituted for the EHI trigger. The low threshold ETFI trigger was essential in determining the efficiencies of the EU, ED and EHI triggers as described in the next section.

II. E. Yield Correction

These data were subjected to an analysis technique similar to that described in an earlier article.[9] Only corrections applied to these data that differ from that article will be described.

II. E. 1. Monte carlo A simpler monte carlo was used for this analysis. This monte carlo determined the geometrical acceptance for each p_T bin by using the same magnetic field map and aperture cuts used in the data analysis. The geometrical acceptance is defined as the fraction of particles produced in a given kinematic bin whose trajectories pass through the experimental aperture. Figures 3a – 3d show the calculated geometrical acceptance for the upper and lower aperture of the SM12 magnet for the $\sqrt{s} = 27.4$ and $\sqrt{s} = 38.8$ GeV data. Instead of incorporating the efficiencies of the various detector elements into this simple monte carlo, the efficiencies of each detector element were determined from data taken concurrently with the less restrictive ETFI trigger. Two factors in the hadron yield were affected by this technique: the tracking efficiency and the calorimeter trigger efficiency.

II. E. 2. Tracking efficiency The tracking efficiency was calculated from the individual wire chamber efficiencies and the track finding algorithm. The calculated tracking efficiency varied between 91% and 96%. The systematic uncertainty in the tracking efficiency was estimated by recalculating the tracking efficiency while varying the wire chamber efficiencies by one standard deviation using the calculated statistical uncertainties in the wire chamber efficiencies.

II. E. 3. Calorimeter trigger efficiency A more complex technique[11,14,15] was used to determine the calorimeter trigger efficiencies and their respective uncertainties. A calorimeter trigger was generated each time the total pulse height of the phototube dynode signals exceeded a set threshold. In the data analysis, the pulse height, PH, associated with a reconstructed track is

$$\mathrm{PH} = \sum_m a_m Q_m f(x),$$

where the sum extends over the calorimeter modules near the track that were included in the hardware trigger, $f(x)$ corrects for light attenuation in the scintillator, Q_m is the charge recorded for module m in the analog-to-digital converters and a_m represents the fact that pulse shapes can differ from module to module. The factors, a_m and $f(x)$, are constructed so that the calculated PH threshold does not depend on the track position at the calorimeter. The calorimeter efficiency, $\epsilon(\mathrm{PH})$, is defined as the number of times a trigger fired in coincidence with the lower threshold ETFI trigger normalized by the number of times the ETFI trigger fired and was fit with an error function (integral of a gaussian distribution):

$$\epsilon(\mathrm{PH}) \equiv erf(\mathrm{PH}; T, \sigma) = \frac{1}{\sqrt{2\pi}\sigma} \int_0^{\mathrm{PH}} dx \exp\left(-\left(\frac{x-T}{\sigma}\right)^2/2\right),$$

where T is the "threshold" of the trigger, the mean of the gaussian. Note that $\epsilon(T) = .5$, and σ is "jitter" in the threshold, the width of the gaussian distribution.

The computed efficiency of the EHI trigger for the 800 GeV/c data is shown in Figure 4. The calorimeter trigger efficiency was computed event-by-event using the PH and the results of the fit to the error function. The systematic uncertainty in the calorimeter trigger efficiency was determined from the estimated uncertainties in the threshold and the jitter of $\pm.5\%$ and $\pm4.6\%(\pm1.0\%$ and $\pm9.2\%)$, respectively, for the 800(400) GeV/c data.

For the majority of the bins, the systematic uncertainty in the single pion cross section is dominated by the uncertainty in the calorimeter efficiency. To eliminate bins at the limits of the overall detector acceptance, all events in each bin were required to have an overall efficiency greater than 5%. The average efficiency of the *worst* bin was 37%.

II. F. Transverse Momentum Resolution

High mass dimuon data taken concurrently with these data using a short(5.6 cm), thin beryllium target yielded a mass resolution of .022 GeV/c^2 for the upsilon[16] and was in good agreement with the momentum scale determined from magnetic field measurements to this accuracy. The calculated resolution in p_T for single hadrons ($\sigma_{p_T}/p_T \approx 2.4\%$) was somewhat worse than the upsilon resolution due to the longer liquid target and the angular divergence of the beam of approximately .68 milliradians(RMS) in the vertical direction, which affects the single particle p_T but not the diparticle invariant mass.

II. G. Track Reconstruction Background

Tracks were selected by a series of cuts on the reconstructed trajectory and the X and Y coordinates at the target Z plane. Two cuts were made on the trajectory inside the SM0-SM12 magnets.

One cut was made on the Y position at the downstream end of the low-angle collimator. The Y position of this aperture point was determined using high mass electron pair data.[17] Electrons provided an accurate guide to locate the collimator, because the tungsten collimator effectively absorbed all incident electrons. The second cut was performed at the Y position of the last lead/tungsten baffle in the SM12 magnet to remove tracks emerging from the steel of the magnet.

These cuts were made two standard deviations (according to the resolution of the track reconstruction) further into the aperture than the determined aperture points. Increasing these cuts to five standard deviations did not significantly change the measured cross sections or particle ratios.

Even with these trajectory cuts, some background events remained in the final target Y distribution. A fit to each distribution with a gaussian and third-order polynomial yielded an estimate of this background. A cut was made at 4(3) standard deviations of the fitted gaussian for the 800(400) GeV/c data and the fitted background subtracted. Figure 5 show the results of one such fit. Note that the width of the distribution is dominated by the tracking resolution and not the width of the incoming proton beam. The complete results are shown in Table 3 where the terms "norm" and "rev" refer to two separate 400 GeV/c data taking periods when the polarities of spectrometer magnets were reversed as a systematic check.

III. Single Pion Cross Sections

The invariant cross sections, $\langle E\frac{d^3\sigma}{dp^3}\rangle \equiv \int E\frac{d^3\sigma}{dp^3}\frac{d^3p}{E} / \int \frac{d^3p}{E}$, for inclusive single pion production averaged over each CMS bin are given in Table 4. Each entry in the table gives the width of the p_T bin, the weighted mean transverse momentum($\langle p_T\rangle \equiv \int p_T E\frac{d^3\sigma}{dp^3}\frac{d^3p}{E} / \int E\frac{d^3\sigma}{dp^3}\frac{d^3p}{E}$) in each bin and the measured cross section with the statistical and systematic uncertainty. Entries are omitted when the measurement is not significantly different from zero at one standard deviation. Figures 6 and 7 show the cross sections for π^+ and π^- , respectively, plotted versus $\langle p_T\rangle$; the errors shown in the figures are the statistical and systematic uncertainty added in quadrature. Note that the transverse momentum that corresponds to the measured average cross section is not identical to $\langle p_T\rangle$; however, the difference is estimated by monte carlo methods to be less than .13 GeV/c for all the measurements shown and does not appreciably affect the shape of the cross section versus p_T .

Shown for comparison at $\sqrt{s} = 27.4\ GeV$ are the results of the Chicago–Princeton(CP) collaboration[2] obtained at $\langle\Theta^*\rangle = 96°$. In addition extrapolations of the charged-pion cross section measurements of the CP and CERN–Columbia–Rockefeller–Saclay (CCRS)[3] collaborations based on fits of the form $E\frac{d^3\sigma}{dp^3} = Af(x_T){p_T}^{-N}$ are shown with the measurements of this experiment at $\sqrt{s} = 38.8\ GeV$.

All results confirm the steep dependence of the single pion cross section on p_T . The lower energy cross sections for both π^+ and π^- in *pp* and *pd* collisions show very good agreement with the CP measurements where the measurements overlap while the $\sqrt{s} = 38.8$ GeV *pp* cross sections are consistent with the CP extrapolation and systematically higher than the CCRS fit.

In the naive parton model, N was predicted to be 4,[18] but experiments[2,3] have measured $N \approx 8$ thus motivating a QCD–based description of high p_T inclusive hadron production. The resulting QCD–improved, parton model (incorporating the Q^2–dependence of the strong coupling, structure functions and fragmentation functions and the intrinsic transverse momentum of the partons in the nucleon) agreed with the measured single pion cross sections for the existing data.[19,20] In addition, N was predicted to decrease at fixed x_T as $\sqrt{s}$ increases in inclusive single hadron production[20] and N was expected to be less than eight in inclusive single jet production. Jet measurements at the ISR and the CERN p-$\bar{p}$ collider indicated $N = 5.3 \pm .2$[21] and inclusive π^o production for $x_T > .3$ were consistent with $N \approx 6$.[22] The predicted and measured scale-dependent variation of N diminishes the ability of the scaling form $Af(x_T){p_T}^{-N}$ to parameterize $E\frac{d^3\sigma}{dp^3}$ over a large range in p_T or $\sqrt{s}$; nevertheless, it is a convenient form that facilitates comparison to other experiments.

The results of fits to the proton–proton data over the entire x_T range ($.19 < x_T < .66$) to the scaling form $E\frac{d^3\sigma}{dp^3} = Af(x_T){p_T}^{-N}$ for two forms of $f(x_T)$ are shown in Table 5. Also shown in the table are the results of the fits by CP and CCRS to their data. Only the diagonal elements of the error matrix are shown for the fits to the measurements of this experiment. There is, however, a strong correlation between b and N, perhaps due to only two values of $\sqrt{s}$ (27.4 and 38.8 GeV) available to this experiment compared to the three values used by CP(19.4, 23.8 and 27.4 GeV) and CCRS(44.8, 52.7 and 62.4 GeV). Both fits give similar values of N for π^+ and π^- production and show an almost identical dependence on p_T as observed by CCRS or CP. Fits restricted to a high x_T range ($x_T > .35$) did not yield significantly different results for N contrary to the results of reference 22.

IV. Particle Ratios

Tables 6, 7 and 8 contain the K/π and p/π production ratios and particle fractions for $\sqrt{s} = 27.4$ GeV *pp* , $\sqrt{s} = 27.4$ GeV *pd* and $\sqrt{s} = 38.8$ GeV *pp* interactions, respectively. Each table entry gives the p_T bin width and the measured particle ratio along with the statistical and estimated systematic uncertainty — only statistical errors are shown in Figures 8 through 12.

IV. A. K^+/π^+ Ratio

In Figures 8a, 8b and 8c, the K^+/π^+ ratios measured in $\sqrt{s} = 27.4$ GeV *pp* and *pd* collisions and $\sqrt{s} = 38.8$ GeV *pp* collisions in this experiment are shown. The results of the CP experiment [2] and the predictions of the Lund model[23] are shown for comparison. The lower energy measurements of both experiments are consistent in the region of overlap; however, the Lund predictions are systematically lower than the measurements.

As noted previously,[24] the roughly constant value of the K^+/π^+ ratio for $p_T > 3$ GeV/c should reflect the relative probability that a valence u-quark picks up an s- or d-quark, P(s)/P(d), in the fragmentation process. A comparison of the average values of the K^+/π^+ ratio for $p_T > 3$ GeV/c as measured in this experiment and predicted by the Lund model is shown in Table 9. One possible explanation of the discrepancy is that pion production by resonance decay is inadequately modelled by Lund.[25] Another possibility[26] is that the standard Lund parameters correctly model the fragmentation process at low z[27] but begin to fail as z increases above $\approx .25$. The measurements of $e^+e^- \rightarrow$ hadrons used to develop the Lund parameters are dominated by a cross section that falls steeply as z increases. On the other hand, high p_T hadrons have been shown[1] to have $\langle z \rangle \approx .8$; therefore, high transverse momentum hadrons probe a region in the fragmentation process poorly examined in electron-positron collisions.

Figure 8d and Table 9 compare the measurements at $\sqrt{s} = 27.4$ and $\sqrt{s} = 38.8$ GeV in pp collisions to predictions by the Split Field Magnet(SFM) collaboration's monte carlo simulation package.[28] The SFM monte carlo (described in detail in references 5, 24 and 29) parameterizes fragmentation distribution generated by the Lund monte carlo at a fixed jet momentum of 10 GeV/c . Three standard Lund features were changed for the SFM predictions: 1) P(s)/P(d) = .45, 2) P(qq)/P(q) = .09 and 3) gluons fragment into quark-anti-quark pairs that fragment independently. The calculations were performed for pp collisions at $\sqrt{s} = 39$ GeV at a production angle of 90° . The agreement is excellent, despite the extrapolation required from the angular region, $\Theta^* \leq 50°$, where the SFM group measured hadroproduction.

IV. B. p/π^+ Ratio

The p/π^+ ratios for $\sqrt{s} = 27.4$ GeV pp and pd collisions are shown in Figures 9a and 9b along with the CP data and Lund predictions. Again there is good agreement with CP and disagreement with the consistently higher predictions of Lund. When the $pp \rightarrow p/\pi^+$ data at both $\sqrt{s} = 27.4$ and $\sqrt{s} = 38.8$ GeV are plotted versus the scaling variable, x_T, as in Figure 10a, the non-scaling behavior of the ratio is observed, in accordance with the supposition[30] that proton production arises from constituent diquark scattering and exhibits the Q^2-dependence of the diquark form factor. This hypothesis is strengthened by the better agreement of the ratios when plotted vs p_T as in Figure 10b if it is supposed that ${p_T}^2 \propto Q^2$.

In Figure 10c the SFM calculation is compared to the data. The dominant source of protons in this calculation is rank 1 fragmentation of quarks. (A "rank 1" parton is a parton from the primary interaction vertex. "Rank 2" partons are produced in the fragmentation of "rank 1" partons.) The predicted p/π^+ ratio depends directly on two phenomenological parameter inputs: the probability of a gluon to fragment to a baryon (or anti-baryon) and the probability of a quark (anti-quark) to fragment to a baryon(anti-baryon). These parameters were set to values of 0.003 and 0.09 for the calculation shown. Eighty percent of the protons are produced in quark fragmentation. No constituent diquark contribution was calculated which explains the inablility of the model to describe the p/π^+ ratio at low p_T .

IV. C. K^-/π^- Ratio

The $\sqrt{s} = 27.4\ GeV$ measurements of K^-/π^- versus p_T shown in Figures 11a and 11b are generally compatible with CP and Lund. When the $\sqrt{s} = 27.4$ and $\sqrt{s} = 38.8\ GeV$ $pp \rightarrow K^-/\pi^-$ measurements are plotted versus x_T as in Figure 12a the x-dependence of the gluon structure function (times the ratio of the fragmentation functions) — generally considered to be the source of K^-at low p_T [24] — is visible. Comparison with the SFM monte carlo in Figure 12c shows good agreement in both shape and magnitude. The data span a kinematic region where the importance of rank 2 quark fragmentation in the production of $K^-$is increasing relative to rank 1 gluon fragmentation. The percentage contribution of these sources — rank 1 gluon fragmentation:rank 1 quark fragmentation:rank 2 quark fragmentation:other — in K^-production are 60:10:25:5 for $x_T > 0.21$ and 40:8:45:7 for $x_T > 0.36$.

V. Summary of Conclusions

1. The inclusive pion production cross sections show a similar steep dependence on p_T as seen by other experiments and parameterized by $E\frac{d^3\sigma}{dp^3} = Af(x_T){p_T}^{-N}$ with $N \approx 8$. No reduction in N was observed for the cross sections restricted to high x_T ($x_T > .35$).
2. For $p_T > 3\ GeV/c$, the constant value of the K^+/π^+ ratio shows the probability of a struck u-quark to pick up an s- or d-quark in the fragmentation process. Good agreement with the predictions of the SFM monte carlo is found, while comparison with the Lund monte carlo reveals some possible inadequacies in the model.
3. The non-scaling behavior of the p/π^+ ratio demonstrates the Q^2–dependence of the form factor of constituent diquarks.
4. Comparison of the K^-/π^- ratio with the SFM monte carlo predictions shows the importance of K^-production by quark–gluon scattering.

ACKNOWLEDGEMENTS

We would like to thank D. Drijard of CERN for providing the SFM calculations. In addition, we wish to thank Jim Peifer and the Fermilab liquid target group who fabricated and maintained the liquid targets. This work was supported in part by the U.S. Department of Energy, the National Science Foundation, the Commissariat a l'Energie Atomique, and the Japan Ministry of Education, Science and Culture(Monbusho).

References

1. A.L.S. Angelis et al., Nucl. Phys. B209, 284(1975).
2. D. Antreasyan et al., Phys. Rev. D19, 764(1979).
3. F.W. Büsser et al., Nucl. Phys. B106, 1(1976).
4. T. Åkesson et al., Nucl. Phys. B246, 408(1984).
5. A. Breakstone et al., Z. Phys. C28, 335 (1985).
6. Andersson et al., Phys. Reports 97, 31(1983); H.–U. Bengtsson and G. Ingleman, CERN preprint LUTP 84-3, Th.3820(1984); T. Sjöstrand, Computer Physics Communications 27, 243(1982).
7. M. Althoff et al., Z. Phys. C17, 5 (1983); H. Aihara et al., Phys. Rev. Letters 53, 2199 (1984); Ch. Berger et al., Nuclear Physics B124, 189 (1983); M. Derrick et al., Phys. Letters 158B, 519 (1985); M. Derrick et al., Phys. Rev. Letters 54, 2568 (1985); W. Bartel et al., Phys. Letters 104B, 325 (1981); P. Baringer et al., ANL-HEP-PR-85-121 (1985).
8. Particle Data Group, Report No. LBL-91, 1985.
9. J.A. Crittenden et al., Phys. Rev. D34, 2584(1986).
10. D.E. Jaffe et al.,Phys. Rev. D38, 1016(1988).
11. D.E. Jaffe, Ph.D. Dissertation, S.U.N.Y. at Stony Brook, 1987.
12. J. Peifer, Fermilab liquid target group, private communication. The purity was determined by accurately weighing a known volume of the liquid.
13. R. Bouclier et al, Nucl. Inst. & Methods 205, 403 (1983); Ph. Mangeot et al, Nucl. Inst. & Methods 216, 79 (1983); M. Adams et al, Nucl. Inst. & Methods 217, 237 (1983); G. Coutrakon, Ph.D. Dissertation, S.U.N.Y. at Stony Brook, 1982; H.D. Glass, Ph.D. Dissertation, S.U.N.Y. at Stony Brook, 1985.
14. P.B. Straub, Ph.D. Dissertation, University of Washington, in preparation.
15. J.A. Crittenden, Ph.D. Dissertation, Columbia University, 1986.
16. R. Gray, Ph.D. Dissertation, University of Washington, 1988.
17. T. Yoshida et al., submitted to Physical Review D.
18. S.M. Berman, J.D. Bjorken and J.B. Kogut, Phys. Rev. D4, 3388(1971).
19. J.M. Owens, E. Reya and M. Glück, Phys. Rev. D18,1501(1978); A.P. Coutogouris, P. Gaskell and S. Papadopoulos, Phys. Rev. D17,2314(1978).
20. R.P. Feynman, R.D. Field and G.C. Fox, Phys. Rev. D18, 3320(1978).
21. T. Åkesson et al., Phys. Lett. 123B, 133(1983).
22. A.G.Clark et al., Phys. Lett. 74B, 267(1978); A.L.S. Angelis et al., Phys. Lett. 79B, 505(1978); C. Kourkoumelis et al., Z. Physik C5, 95(1980).
23. The standard PYTHIA version 4.2 and JETSET version 6.2 of the Lund program were used. In the figures the horizontal error bars of the Lund points show the bin width. In these versions the strangeness suppression factor, P(s)/P(d), is .3 and the diquark suppression factor, P(qq)/P(q), is .1. To obtain the Lund model results for *pd* interactions, the predicted hadron production rates in *pn* and *pp* collisions was simply summed.
24. A. Breakstone et al., Phys. Lett. 135B, 510(1984).
25. A. Seiden, "Comparison of Jet Fragmentation in Various Processes", Invited Paper, 6th International Conference on Proton Antiproton Physics, Aachen, Germany, July 1986.

26. G.D.Cowan, Ph.D. Dissertation, University of California,
Report No. LBL-24715(1988); H. Aihara et al. (TPC/Two-Gamma Collaboration),
Report No. LBL-24896(1988).
27. The fragmentation variable, z, is defined as the fraction of the parton momentum carried by the observed hadron. In electron-positron collisions this definition reduces to the ratio of the hadron momentum to the beam momentum.
28. D. Drijard, CERN, private communication.
29. D. Drijard et al., Phys. Lett. 121B, 433(1983); A. Breakstone et al., Phys. Lett. 135B, 505(1984).
30. S. Ekelin and S. Fredriksson, Phys. Lett. 149B, 509(1984)

TABLE CAPTIONS

1. The reactions and kinematic ranges of the data.
2. The total number of protons on target and integrated luminosity for each data set. Only statistical uncertainties are shown in the table; the ±2% [limit of error] systematic uncertainty in the *pd* luminosity is not shown.
3. The calculated background fraction of the reconstructed target tracks.
4. The values of the single positive and negative pion inclusive invariant cross section per nucleus as a function of transverse momentum for a) pp $\sqrt{s} = 27.4$ GeV , b) pd $\sqrt{s} = 27.4$ GeV and c) pp $\sqrt{s} = 38.8$ GeV . The data are averaged over the range in $\cos\Theta^*$ given in Table 1 and the stated transverse momentum bin. Each entry contains the measured cross section followed by the statistical and systematic uncertainty. The ±2% systematic uncertainty in the *pd* cross sections due the contamination of the "deuterium" target is not included in the entries in Table 4b.
5. The values of the fit parameters b and N for the invariant cross section per nucleus for positive and negative pions for this experiment, Reference 2(CP) and Reference 3(CCRS). The functional form of the fit is $E\frac{d^3\sigma}{dp^3} = Af(x_T){p_T}^{-N}$ where two forms of $f(x_T)$ were used to facilitate comparison between experiments. The tables show the range in x_T over which the cross section was fit by each experiment. In the table DOF means degrees of freedom.
6. The particle ratios(a) and fractions(b) as a function of transverse momentum for the pp $\sqrt{s} = 27.4$ GeV data. Each entry in a) contains the measured particle ratio, the statistical and systematic error. Each entry in b) contains the measured particle fraction, the statistical and systematic error. The sign of the systematic uncertainty reflects the correlation between the three particle fractions (each hadron is either a π,Kor p).
7. The particle ratios(a) and fractions(b) as a function of transverse momentum for the pd $\sqrt{s} = 27.4$ GeV data.
8. The particle ratios(a) and fractions(b) as a function of transverse momentum for the pp $\sqrt{s} = 38.8$ GeV data.
9. Comparison of the measured and predicted K^+/π^+ ratio with statistical uncertainties only for $p_T > 3$ GeV/c .

Table 1

Reaction	$\sqrt{s}$ (Gev)	p_T range (Gev/c)	$x_\perp$ range	$\cos\Theta^*$ range
$pp(d) \rightarrow hX$	27.4	5.2 - 9.0	.38 to .66	$-.3$ to .3
$pp \rightarrow hX$	38.8	3.6 - 11.0	.19 to .57	$-.2$ to .2

Table 2

Data set	Total protons on target	Integrated luminosity per target nucleus (pb^{-1})
400 *GeV pp*	$(5.09 \pm .19) \times 10^{14}$	$436. \pm 23.$
400 *GeV pd*	$(7.80 \pm .29) \times 10^{14}$	$761. \pm 39.$
800 *GeV pp*	$(7.17 \pm .45) \times 10^{14}$	$615. \pm 32.$

Table 3

Data set	Negative particles	Positive particles
800 *GeV pp*	$.041 \pm .003$	$.038 \pm .002$
400 *GeV pp* (norm)	$.071 \pm .018$	$.074 \pm .009$
400 *GeV pp* (rev)	$.096 \pm .024$	$.096 \pm .024$
400 *GeV pd*	$.033 \pm .004$	$.104 \pm .006$

Table 4a

p_T bin Gev/c	$\langle p_T \rangle$ Gev/c	$E\frac{d^3\sigma}{dp^3}$ $(pp \rightarrow \pi^- X)$ $[\mathrm{pb}/(GeV^2/c^3)]$
5.2 – 5.7	5.60	$(2.37 \pm 1.03 \pm 0.19) \times 10^1$
5.7 – 6.2	5.97	$7.33 \pm 2.12 \pm 0.46$
6.2 – 6.7	6.35	$1.97 \pm 0.84 \pm 0.16$

p_T bin Gev/c	$\langle p_T \rangle$ Gev/c	$E\frac{d^3\sigma}{dp^3}$ $(pp \rightarrow \pi^+ X)$ $[\mathrm{pb}/(GeV^2/c^3)]$
5.2 – 5.7	5.52	$(3.41 \pm 1.78 \pm 0.41) \times 10^1$
5.7 – 6.2	5.95	$(1.53 \pm 0.31 \pm 0.09) \times 10^1$
6.7 – 7.2	6.92	$1.05 \pm 0.56 \pm 0.09$
7.2 – 7.7	7.56	$(2.15 \pm 1.32 \pm 0.45) \times 10^{-1}$
7.7 – 9.0	8.10	$(1.52 \pm 0.94 \pm 0.67) \times 10^{-2}$

Table 4b

p_T bin Gev/c	$\langle p_T \rangle$ Gev/c	$E\frac{d^3\sigma}{dp^3}$ $(pd \rightarrow \pi^- X)$ $[\mathrm{pb}/(GeV^2/c^3)]$
5.2 – 5.7	5.57	$(8.73 \pm 2.12 \pm 0.58) \times 10^1$
5.7 – 6.2	5.96	$(1.46 \pm 0.20 \pm 0.08) \times 10^1$
6.2 – 6.7	6.44	$3.67 \pm 0.61 \pm 0.23$
6.7 – 7.2	6.83	$1.16 \pm 0.32 \pm 0.08$
7.2 – 7.7	7.43	$(4.60 \pm 1.07 \pm 0.30) \times 10^{-1}$
7.7 – 9.0	8.04	$(1.66 \pm 0.40 \pm 0.30) \times 10^{-2}$

p_T bin Gev/c	$\langle p_T \rangle$ Gev/c	$E\frac{d^3\sigma}{dp^3}$ $(pd \rightarrow \pi^+ X)$ $[\mathrm{pb}/(GeV^2/c^3)]$
5.2 – 5.7	5.57	$(7.87 \pm 1.56 \pm 0.77) \times 10^1$
5.7 – 6.2	5.95	$(2.15 \pm 0.24 \pm 0.13) \times 10^1$
6.2 – 6.7	6.41	$7.07 \pm 0.90 \pm 0.47$
6.7 – 7.2	7.02	$(9.23 \pm 3.29 \pm 0.98) \times 10^{-1}$
7.2 – 7.7	7.46	$(4.77 \pm 0.87 \pm 0.27) \times 10^{-1}$
7.7 – 9.0	8.13	$(2.97 \pm 0.64 \pm 0.61) \times 10^{-2}$

Table 4c

p_T bin Gev/c	$\langle p_T \rangle$ Gev/c	$E\frac{d^3\sigma}{dp^3}$ $(pp \rightarrow \pi^-\mathrm{X})$ $[\mathrm{pb}/(GeV^2/c^3)]$
3.6 – 4.0	3.87	$(1.00 \pm 0.18 \pm 0.08) \times 10^4$
4.0 – 4.5	4.23	$(3.26 \pm 0.27 \pm 0.24) \times 10^3$
4.5 – 5.0	4.71	$(9.92 \pm 0.83 \pm 0.77) \times 10^2$
5.0 – 5.5	5.17	$(2.83 \pm 0.31 \pm 0.27) \times 10^2$
5.5 – 6.0	5.63	$(1.06 \pm 0.14 \pm 0.09) \times 10^2$
6.0 – 6.5	6.29	$(3.58 \pm 0.78 \pm 0.31) \times 10^1$
7.0 – 7.5	7.22	$1.85 \pm 0.68 \pm 0.16$
7.5 – 8.0	7.71	$1.60 \pm 0.44 \pm 0.12$
8.0 – 9.0	8.50	$(4.52 \pm 1.73 \pm 0.43) \times 10^{-1}$

p_T bin Gev/c	$\langle p_T \rangle$ Gev/c	$E\frac{d^3\sigma}{dp^3}$ $(pp \rightarrow \pi^+\mathrm{X})$ $[\mathrm{pb}/(GeV^2/c^3)]$
3.6 – 4.0	3.89	$(1.62 \pm 0.33 \pm 0.13) \times 10^4$
4.0 – 4.5	4.23	$(4.62 \pm 0.38 \pm 0.33) \times 10^3$
4.5 – 5.0	4.73	$(1.40 \pm 0.12 \pm 0.11) \times 10^3$
5.0 – 5.5	5.20	$(4.42 \pm 0.40 \pm 0.39) \times 10^2$
5.5 – 6.0	5.64	$(1.66 \pm 0.19 \pm 0.14) \times 10^2$
6.0 – 6.5	6.14	$(5.87 \pm 0.88 \pm 0.45) \times 10^1$
6.5 – 7.0	6.64	$(1.35 \pm 0.16 \pm 0.08) \times 10^1$
7.0 – 7.5	7.26	$5.72 \pm 0.81 \pm 0.36$
7.5 – 8.0	7.82	$2.64 \pm 0.68 \pm 0.16$
8.0 – 9.0	8.44	$(6.78 \pm 1.87 \pm 0.58) \times 10^{-1}$
9.0 –11.0	9.65	$(5.87 \pm 4.20 \pm 1.00) \times 10^{-2}$

Table 5

This experiment (.19 < x_T < .66)				
$f(x_T)$	b	N	χ^2/DOF	
$(1-x_T)^b$	10.8 ± 0.3	8.4 ± 0.1	16.1/13	π^+
$(1-x_T)^b$	10.6 ± 0.6	8.4 ± 0.1	9.4/9	π^-

CP collaboration (.35 < x_T < .64)				
$f(x_T)$	b	N	χ^2/DOF	
$(1-x_T)^b$	9.0 ± 0.5	8.2 ± 0.5	17/8	π^+
$(1-x_T)^b$	9.5 ± 0.5	8.5 ± 0.5	5.8/7	π^-

This experiment (.19 < x_T < .66)				
$f(x_T)$	b	N	χ^2/DOF	
e^{-bx_T}	$20.4 \pm .4$	7.0 ± 0.1	21.5/13	π^+
e^{-bx_T}	17.2 ± 1.0	7.7 ± 0.2	10.4/9	π^-

CCRS collaboration(.11 < x_T < .36)				
$f(x_T)$	b	N	χ^2/DOF	
e^{-bx_T}	15.4 ± 1.2	$7.5 \pm .17$	72/63	π^+
e^{-bx_T}	16.1 ± 1.2	7.86 ± 0.30	70/64	π^-

Table 6a

p_T bin Gev/c	K^+/π^+	p/π^+
5.2- 5.7	.418±.058±.003	.226±.042±.006
5.7- 6.2	.423±.037±.007	.236±.027±.004
6.2- 6.7	.407±.047±.008	.133±.029±.004
6.7- 7.2	.383±.061±.017	.087±.033±.023
7.2- 7.7	.487±.127±.021	.208±.076±.011
7.7- 9.0	.725±.248±.230	—
	K^-/π^-	$\overline{p}/\pi^-$
5.2- 5.7	.114±.034±.002	.165±.043±.005
5.7- 6.2	.125±.024±.005	.085±.024±.003
6.2- 6.7	.081±.025±.007	.042±.026±.003
6.7- 7.2	.095±.044±.014	—
7.2- 7.7	.058±.055±.014	.068±.058±.007

Table 6b

p_T bin Gev/c	π^+/h^+	K^+/h^+	p/h^+
5.2- 5.7	.608 ±.040 ∓0.002	.254 ±.030 ∓0.000	.137 ±.023 ±0.002
5.7- 6.2	.603 ±.025 ∓0.002	.255 ±.019 ±0.002	.142 ±.015 ∓0.000
6.2- 6.7	.649 ±.036 ∓0.003	.264 ±.026 ±0.003	.086 ±.018 ±0.000
6.7- 7.2	.680 ±.051 ±0.004	.260 ±.035 ±0.007	.060 ±.022 ∓0.011
7.2- 7.7	.590 ±.080 ∓0.006	.287 ±.060 ±0.006	.123 ±.041 ∓0.000
7.7- 9.0	.565 ±.115 ∓0.061	.410 ±.103 ±0.068	.025 ±.051 ∓0.007
	π^-/h^-	K^-/h^-	$\overline{p}/h^-$
5.2- 5.7	.782 ±.061 ∓0.002	.089 ±.025 ∓0.000	.129 ±.030 ±0.002
5.7- 6.2	.826 ±.043 ∓0.002	.104 ±.019 ±0.002	.071 ±.019 ∓0.000
6.2- 6.7	.891 ±.063 ∓0.003	.072 ±.022 ±0.003	.037 ±.023 ∓0.000
6.7- 7.2	.910 ±.101 ±0.006	.086 ±.038 ±0.007	.004 ±.040 ∓0.013
7.2- 7.7	.888 ±.161 ∓0.006	.052 ±.047 ±0.006	.060 ±.049 ∓0.000
7.7- 9.0	.655 ±.287 ∓0.056	.184 ±.180 ±0.062	.161 ±.157 ∓0.006

Table 7a

p_T bin Gev/c	K^+/π^+	p/π^+
5.2- 5.7	.440±.068±.003	.161±.045±.006
5.7- 6.2	.418±.033±.025	.132±.021±.014
6.2- 6.7	.369±.035±.006	.140±.023±.003
6.7- 7.2	.374±.036±.016	.108±.019±.021
7.2- 7.7	.391±.050±.019	.089±.025±.009
7.7- 9.0	.429±.088±.186	.146±.048±.098
	K^-/π^-	$\overline{p}/\pi^-$
5.2- 5.7	.079±.017±.002	.066±.020±.004
5.7- 6.2	.092±.012±.005	.067±.014±.003
6.2- 6.7	.084±.015±.006	.023±.014±.003
6.7- 7.2	.078±.018±.011	—
7.2- 7.7	.028±.016±.013	—

Table 7b

p_T bin Gev/c	π^+/h^+	K^+/h^+	p/h^+
5.2- 5.7	.625 ±.049 ∓0.002	.275 ±.036 ∓0.000	.100 ±.026 ±0.002
5.7- 6.2	.645 ±.025 ∓0.007	.270 ±.018 ±0.009	.085 ±.013 ∓0.002
6.2- 6.7	.663 ±.030 ∓0.002	.245 ±.020 ±0.002	.092 ±.014 ±0.000
6.7- 7.2	.675 ±.032 ±0.003	.252 ±.021 ±0.007	.073 ±.013 ∓0.011
7.2- 7.7	.676 ±.043 ∓0.006	.264 ±.028 ±0.006	.060 ±.016 ∓0.000
7.7- 9.0	.635 ±.068 ∓0.056	.272 ±.046 ±0.062	.093 ±.029 ∓0.006
	π^-/h^-	K^-/h^-	$\overline{p}/h^-$
5.2- 5.7	.873 ±.042 ∓0.002	.069 ±.014 ∓0.000	.057 ±.017 ±0.002
5.7- 6.2	.863 ±.028 ∓0.002	.079 ±.010 ±0.002	.058 ±.011 ∓0.000
6.2- 6.7	.903 ±.039 ∓0.003	.076 ±.013 ±0.002	.021 ±.012 ±0.000
6.7- 7.2	.920 ±.048 ±0.003	.072 ±.016 ±0.007	.007 ±.014 ∓0.010
7.2- 7.7	.968 ±.073 ∓0.006	.027 ±.015 ±0.006	.004 ±.017 ∓0.000
7.7- 9.0	.931 ±.138 ∓0.059	.028 ±.029 ±0.066	.041 ±.040 ∓0.007

Table 8a

p_T bin Gev/c	K^+/π^+	p/π^+
3.6- 4.0	.530±.041±.014	.355±.030±.010
4.0- 4.5	.481±.023±.013	.206±.016±.009
4.5- 5.0	.470±.034±.005	.163±.022±.003
5.0- 5.5	.559±.057±.004	.110±.029±.004
5.5- 6.0	.433±.045±.006	.105±.023±.004
6.0- 6.5	.484±.036±.007	.084±.014±.004
6.5- 7.0	.467±.035±.019	.050±.011±.011
7.0- 7.5	.562±.051±.036	.095±.018±.023
7.5- 8.0	.447±.050±.033	.053±.015±.017
8.0- 9.0	.453±.051±.112	.064±.017±.058
9.0-11.0	.494±.099±.147	.021±.015±.075
	K^-/π^-	$\bar{p}/\pi^-$
3.6- 4.0	.296±.029±.010	.063±.021±.007
4.0- 4.5	.279±.019±.010	.051±.014±.007
4.5- 5.0	.270±.027±.004	—
5.0- 5.5	.175±.029±.003	.030±.017±.003
5.5- 6.0	.172±.029±.004	—
6.0- 6.5	.138±.023±.001	.016±.009±.001
6.5- 7.0	.104±.022±.014	—
7.0- 7.5	.145±.032±.026	—
7.5- 8.0	.081±.026±.039	.033±.016±.020
8.0- 9.0	.087±.031±.084	—
9.0-11.0	.061±.049±.103	—

Table 8b

p_T bin Gev/c	π^+/h^+	K^+/h^+	p/h^+
3.6- 4.0	.531 ±.022 ∓0.004	.281 ±.018 ±0.003	.188 ±.014 ±0.001
4.0- 4.5	.593 ±.015 ∓0.004	.285 ±.012 ±0.003	.122 ±.009 ±0.001
4.5- 5.0	.612 ±.022 ∓0.001	.288 ±.017 ±0.002	.100 ±.013 ∓0.000
5.0- 5.5	.599 ±.034 ∓0.002	.335 ±.027 ±0.000	.066 ±.017 ±0.000
5.5- 6.0	.650 ±.035 ∓0.002	.281 ±.024 ±0.002	.068 ±.014 ∓0.000
6.0- 6.5	.638 ±.026 ∓0.002	.309 ±.019 ±0.003	.054 ±.009 ∓0.001
6.5- 7.0	.659 ±.027 ∓0.005	.308 ±.019 ±0.007	.033 ±.007 ∓0.002
7.0- 7.5	.604 ±.031 ∓0.012	.339 ±.024 ±0.010	.057 ±.010 ±0.002
7.5- 8.0	.667 ±.038 ∓0.011	.298 ±.027 ±0.011	.035 ±.010 ±0.000
8.0- 9.0	.659 ±.037 ∓0.035	.299 ±.027 ±0.039	.042 ±.011 ∓0.003
9.0-11.0	.660 ±.067 ∓0.047	.326 ±.051 ±0.050	.014 ±.010 ∓0.002

	π^-/h^-	K^-/h^-	$\overline{p}/h^-$
3.6- 4.0	.736 ±.030 ∓0.004	.218 ±.019 ±0.003	.047 ±.015 ±0.001
4.0- 4.5	.752 ±.021 ∓0.004	.210 ±.013 ±0.003	.038 ±.010 ±0.001
4.5- 5.0	.779 ±.032 ∓0.001	.210 ±.019 ±0.002	.011 ±.015 ∓0.000
5.0- 5.5	.830 ±.049 ∓0.002	.145 ±.022 ±0.000	.025 ±.014 ±0.000
5.5- 6.0	.853 ±.049 ∓0.001	.146 ±.023 ±0.002	.001 ±.022 ∓0.000
6.0- 6.5	.867 ±.045 ±0.000	.119 ±.018 ±0.000	.014 ±.008 ∓0.000
6.5- 7.0	.900 ±.050 ∓0.005	.094 ±.018 ±0.007	.007 ±.007 ∓0.002
7.0- 7.5	.873 ±.059 ∓0.012	.126 ±.026 ±0.010	.001 ±.023 ±0.002
7.5- 8.0	.898 ±.065 ∓0.018	.073 ±.022 ±0.017	.029 ±.015 ±0.000
8.0- 9.0	.913 ±.065 ∓0.037	.080 ±.027 ±0.040	.007 ±.016 ∓0.004
9.0-11.0	.940 ±.127 ∓0.047	.057 ±.045 ±0.050	.003 ±.028 ∓0.002

Table 9

Reaction	This experiment	Lund prediction	SFM prediction
$pp\ \sqrt{s} = 27.4\ GeV$	$.47 \pm .06$	$.32 \pm .02$	—
$pd\ \sqrt{s} = 27.4\ GeV$	$.40 \pm .04$	$.32 \pm .02$	—
$pp\ \sqrt{s} = 38.8\ GeV$	$.49 \pm .04$	$.33 \pm .02$	$.49 \pm .04$

FIGURE CAPTIONS

1. The E605 spectrometer.
2. Enlarged view of SM0 and SM12 showing the tungsten collimator and lead/tungsten baffles.
3. The calculated geometric acceptance as a function of transverse momentum for the a) upper and b) lower aperture for the $\sqrt{s} = 27.4\ GeV$ data and for the c) upper and d) lower aperture for the $\sqrt{s} = 38.8\ GeV$ data. The horizontal error bars show the width of the transverse momentum bin; the vertical error bars indicate the statistical uncertainty of the monte carlo results.
4. The calculated efficiency of the EHI calorimeter trigger.
5. The target Y-distribution for positive particles showing the gaussian and polynomial fits.
6. The single positive pion inclusive invariant cross sections per nucleus as a function of transverse momentum for a) $pp\ \sqrt{s} = 27.4\ GeV$, b) $pd\ \sqrt{s} = 27.4\ GeV$ and c) $pp\ \sqrt{s} = 38.8\ GeV$. The $\pm 2\%$ systematic uncertainty in the pd cross sections due to target contamination is not included in Figure 5b.
7. The single negative pion inclusive invariant cross sections per nucleus as a function of transverse momentum for a) $pp\ \sqrt{s} = 27.4\ GeV$, b) $pd\ \sqrt{s} = 27.4\ GeV$ and c) $pp\ \sqrt{s} = 38.8\ GeV$. The $\pm 2\%$ systematic uncertainty in the pd cross sections due to target contamination is not included in Figure 6b.
8. The relative K^+/π^+ production rate as a function of transverse momentum for a) $pp\ \sqrt{s} = 27.4\ GeV$, b) $pd\ \sqrt{s} = 27.4\ GeV$ and c) $pp\ \sqrt{s} = 38.8\ GeV$, and d) the measured relative K^+/π^+ production rate at $\sqrt{s} = 38.8\ GeV$ compared to the SFM monte carlo. The horizontal error bars show the bin width used for the monte carlo points.
9. The relative p/π^+ production rate as a function of transverse momentum for a) $pp\ \sqrt{s} = 27.4\ GeV$, b) $pd\ \sqrt{s} = 27.4\ GeV$ and c) $pp\ \sqrt{s} = 38.8\ GeV$.
10. The relative p/π^+ production rate in pp collisions as a function of a) the scaled transverse momentum, b) the transverse momentum and c) the transverse momentum at $\sqrt{s} = 38.8\ GeV$ compared to the SFM monte carlo.
11. The relative K^-/π^- production rate as a function of transverse momentum for a) $pp\ \sqrt{s} = 27.4\ GeV$, b) $pd\ \sqrt{s} = 27.4\ GeV$ and c) $pp\ \sqrt{s} = 38.8\ GeV$.
12. The relative K^-/π^- production rate in pp collisions as a function of a) the scaled transverse momentum, b) the transverse momentum and c) the transverse momentum at $\sqrt{s} = 38.8\ GeV$ compared to the SFM monte carlo.

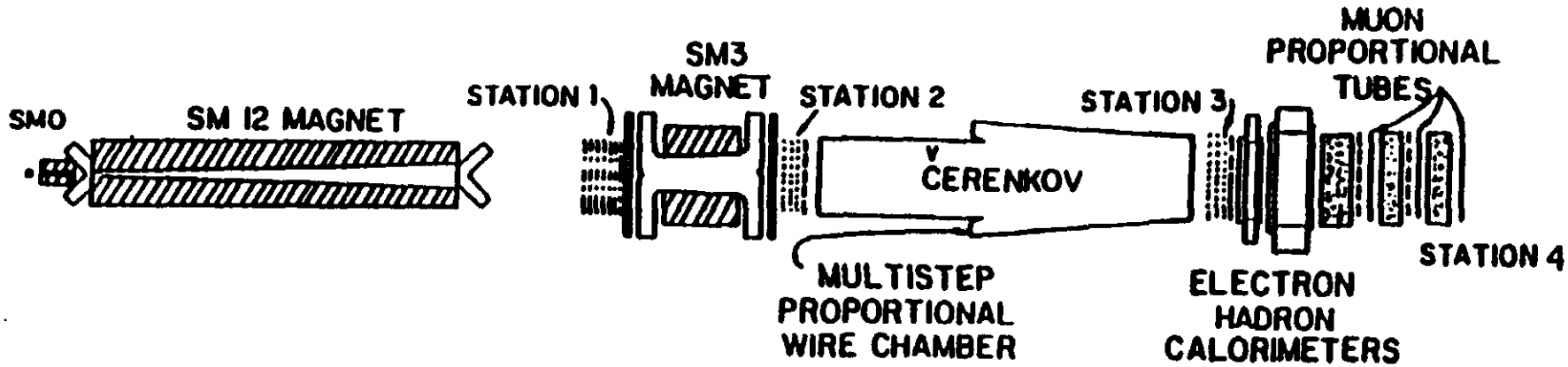

PLAN VIEW E-605

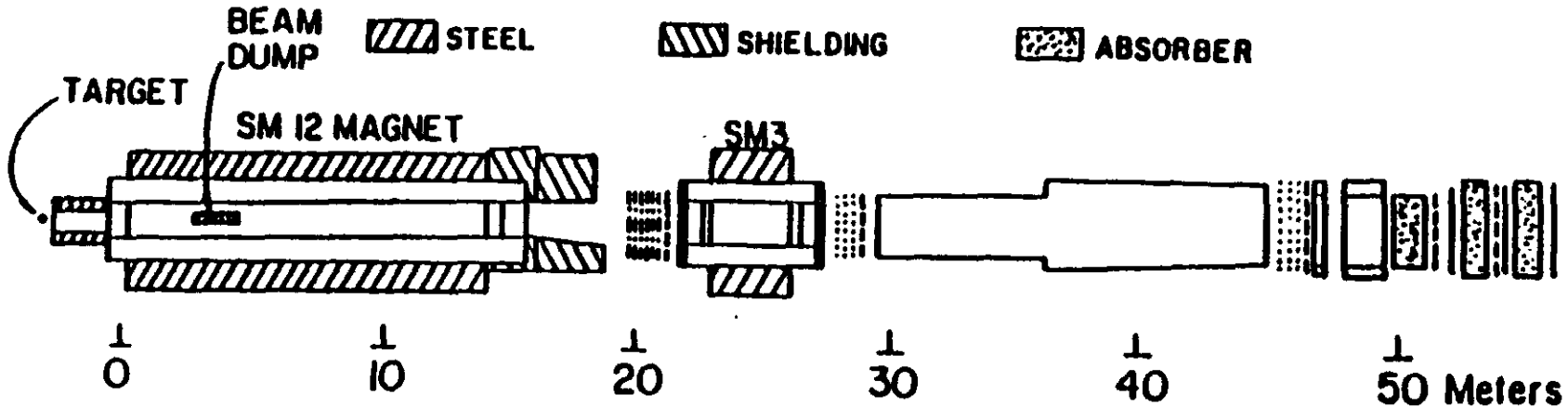

ELEVATION SECTION E-605

Figure 1

····· DRIFT CHAMBER

-·-·- PROPORTIONAL CHAMBER

----- COUNTER BANK

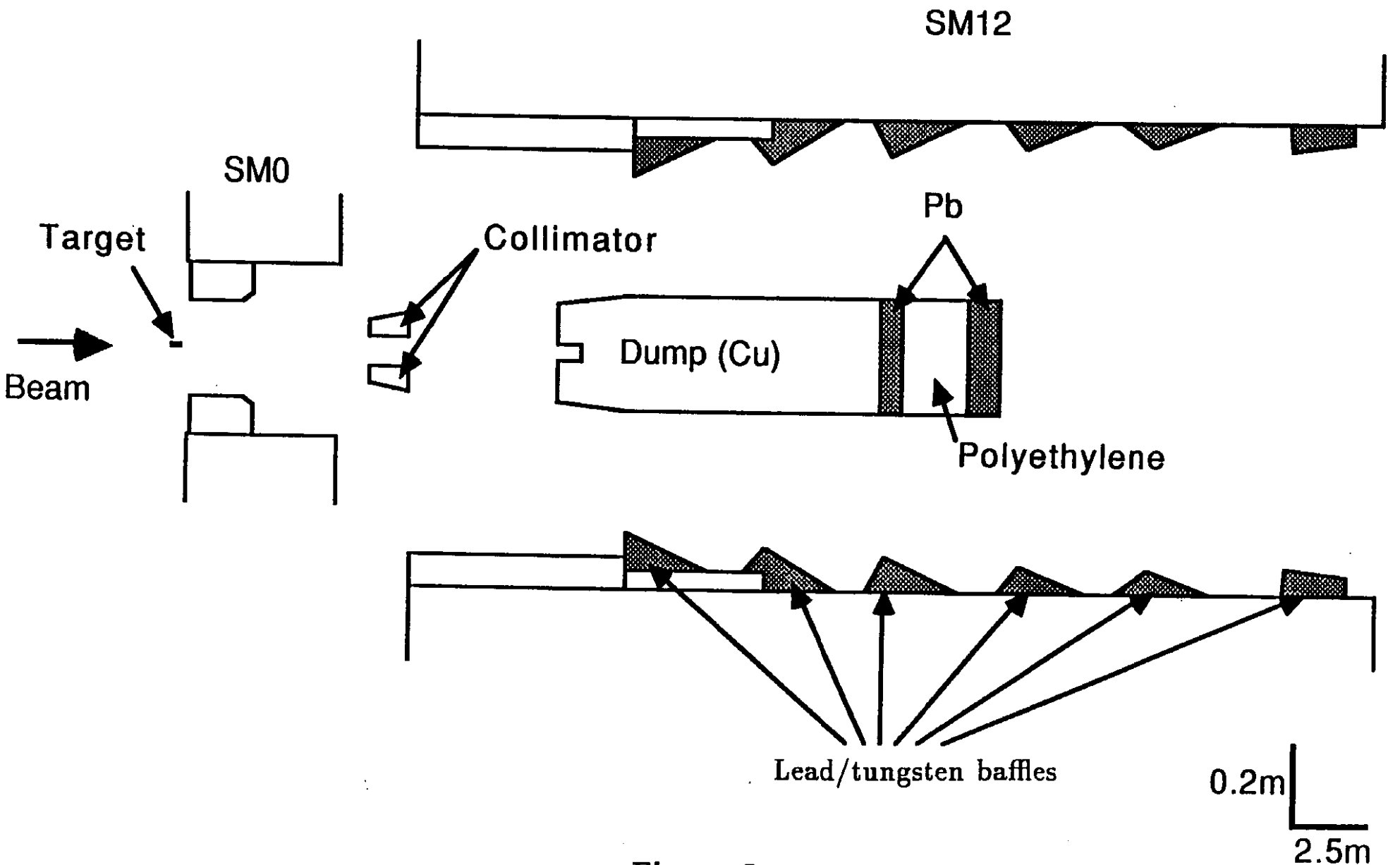
SM12
SM0
Target
Collimator
Pb
Dump (Cu)
Beam
Polyethylene
Lead/tungsten baffles
0.2m
2.5m

Figure 2

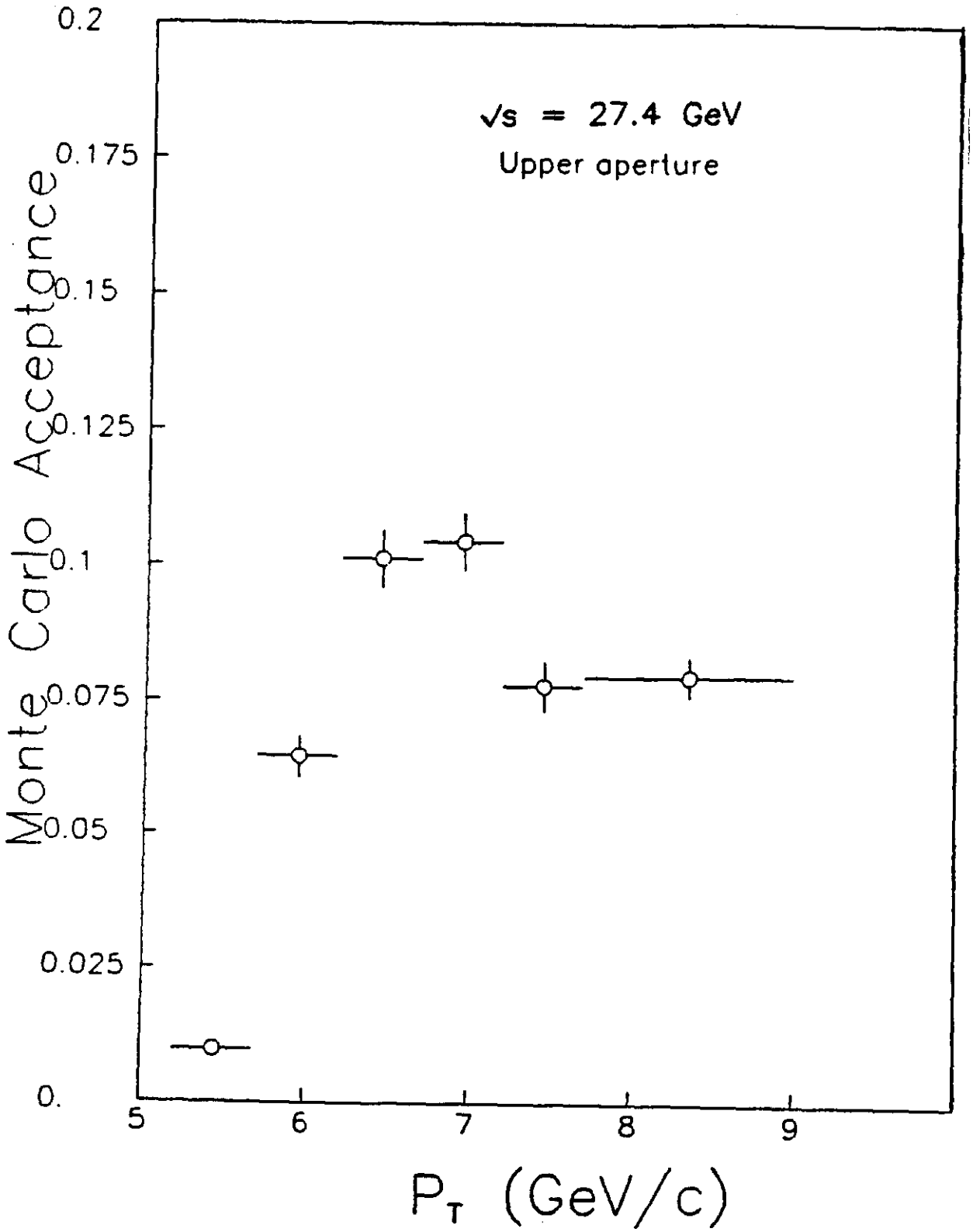
√s = 27.4 GeV
Upper aperture
Monte Carlo Acceptance
0.2
0.175
0.15
0.125
0.1
0.075
0.05
0.025
0.
5
6
7
8
9
P_T (GeV/c)

Figure 3a

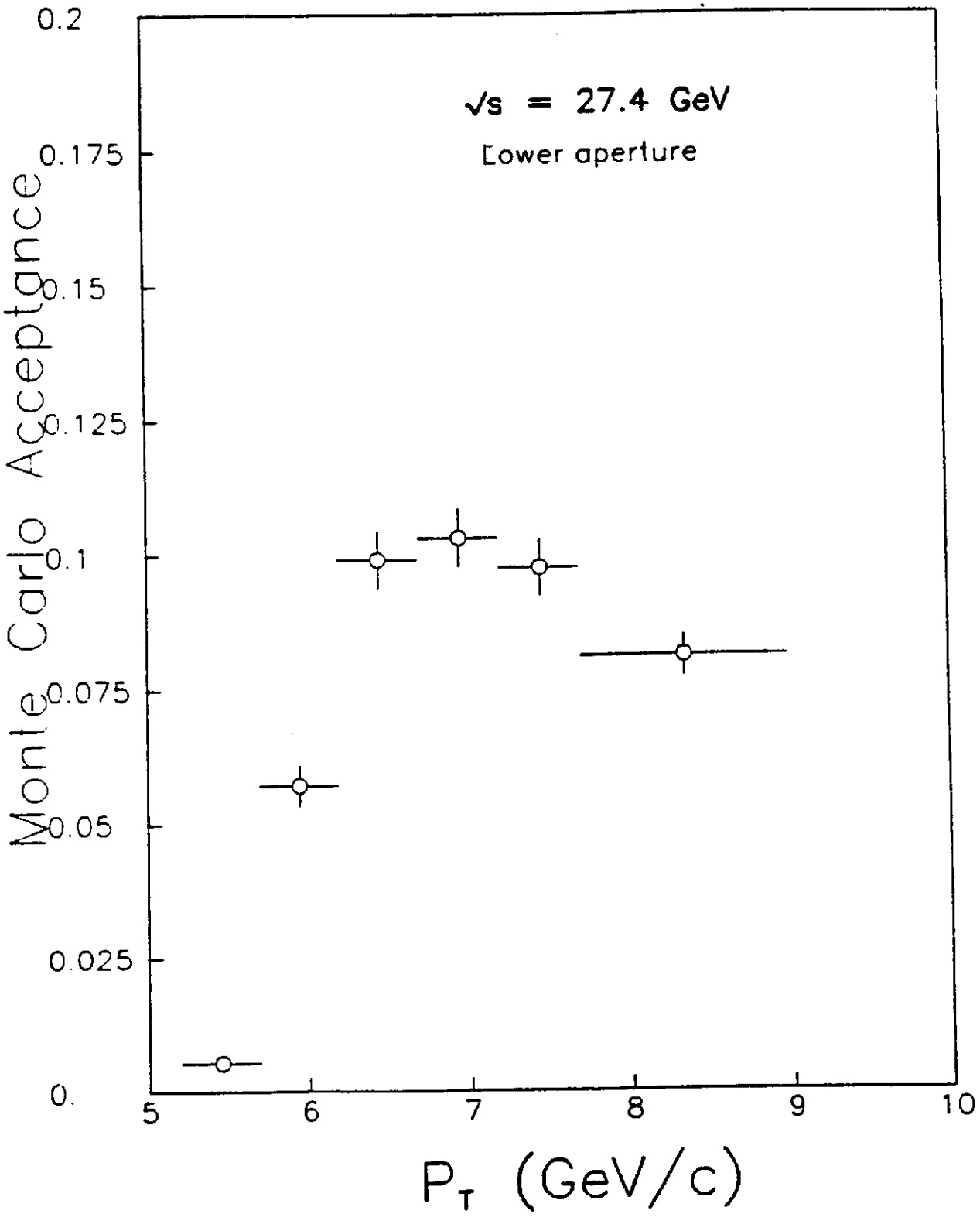
√s = 27.4 GeV
Lower aperture
Monte Carlo Acceptance
0.2
0.175
0.15
0.125
0.1
0.075
0.05
0.025
0.
5
6
7
8
9
10
P_T (GeV/c)

Figure 3b

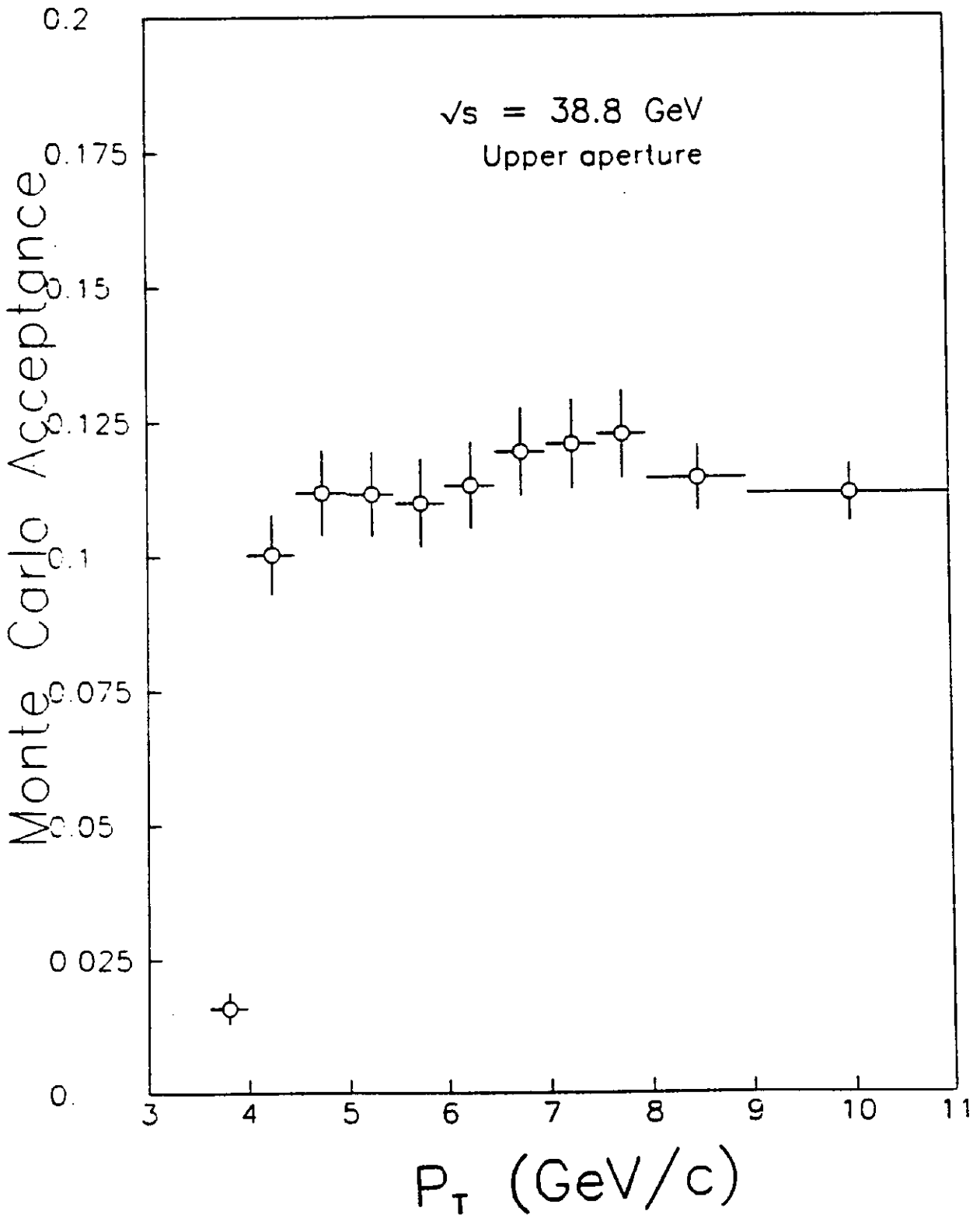
√s = 38.8 GeV
Upper aperture
Monte Carlo Acceptance
0.2
0.175
0.15
0.125
0.1
0.075
0.05
0.025
0
3
4
5
6
7
8
9
10
11
P_T (GeV/c)

Figure 3c

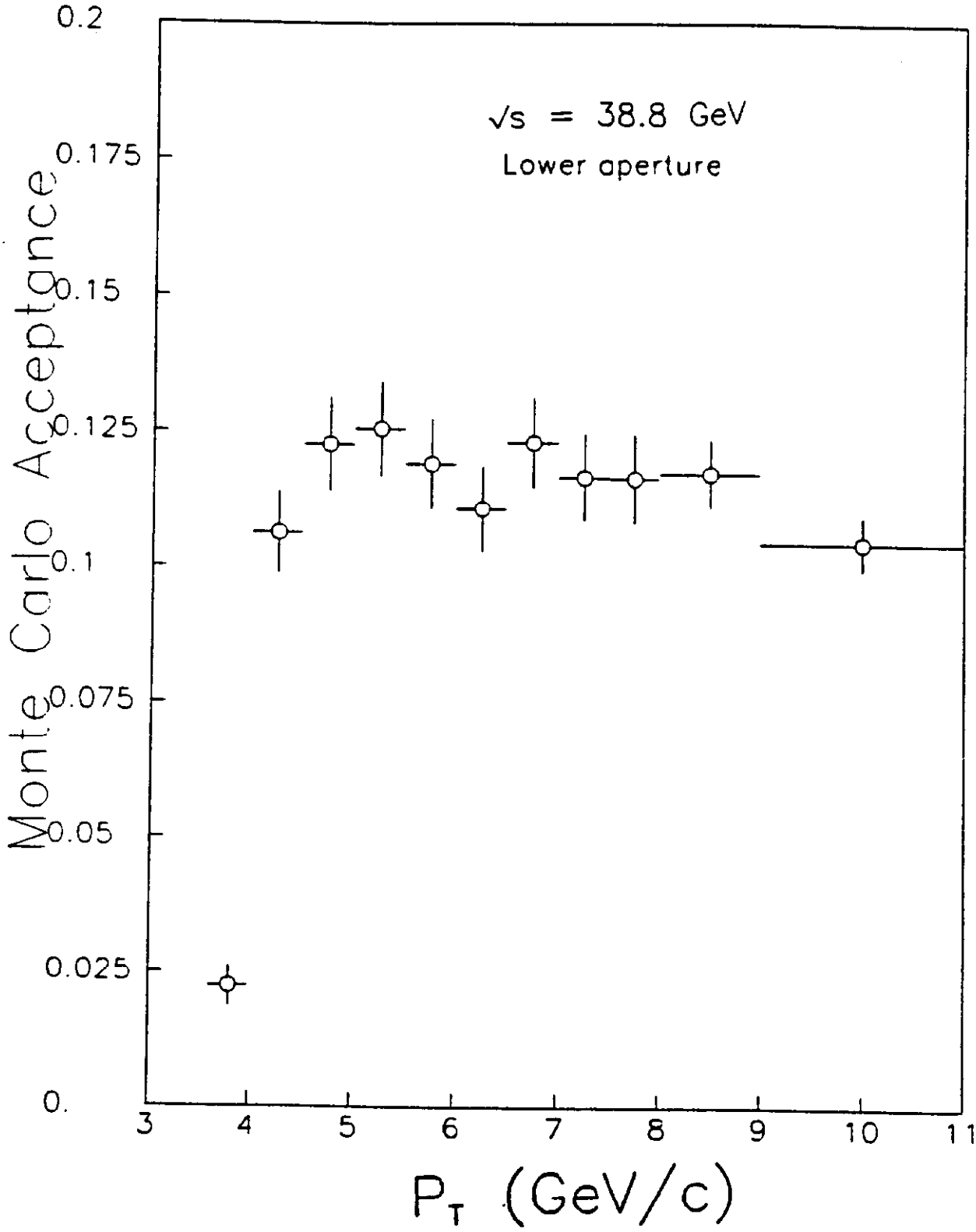
√s = 38.8 GeV
Lower aperture
Monte Carlo Acceptance
0.2
0.175
0.15
0.125
0.1
0.075
0.05
0.025
0.
3
4
5
6
7
8
9
10
11
P_T (GeV/c)

Figure 3d

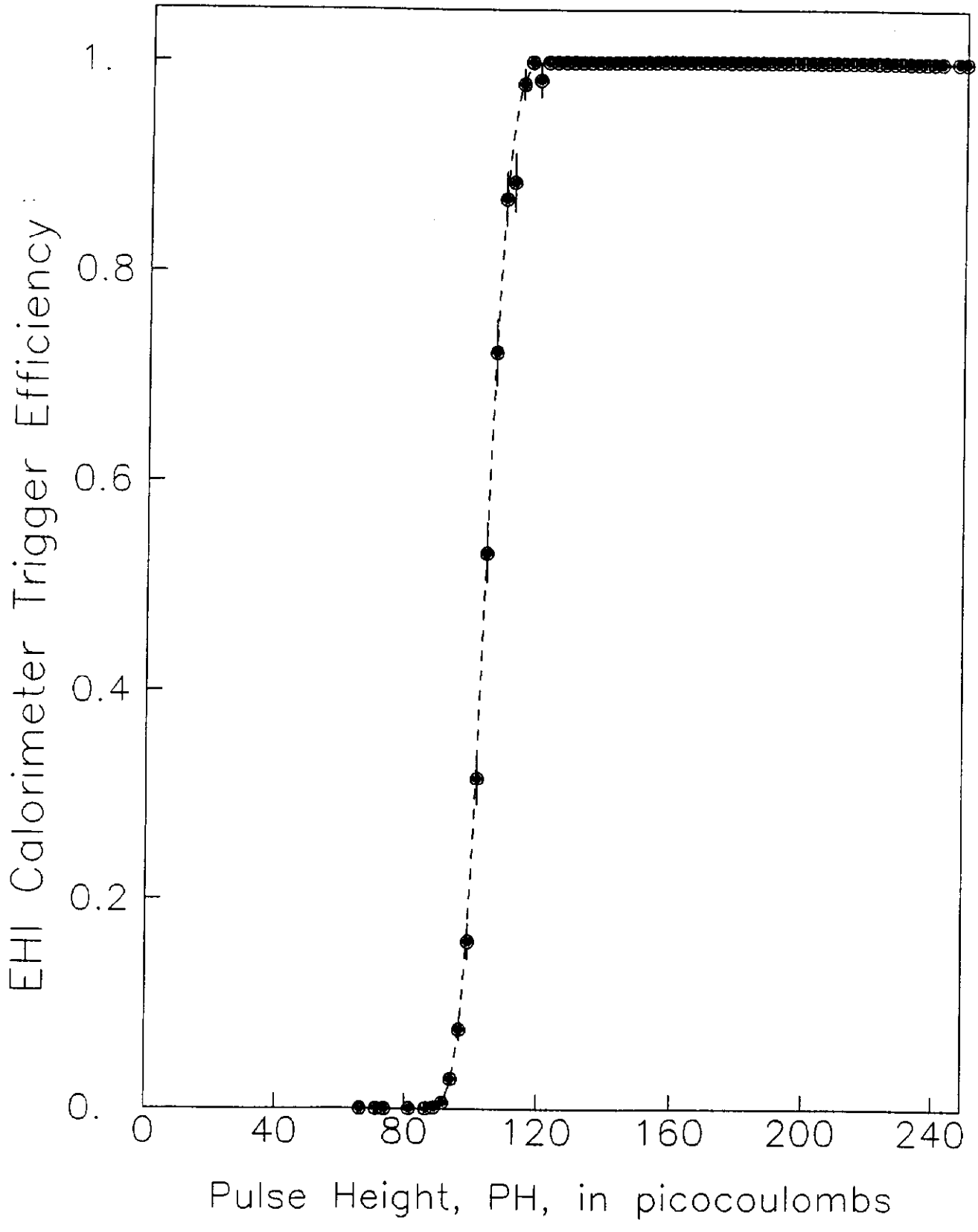
EHI Calorimeter Trigger Efficiency
1.
0.8
0.6
0.4
0.2
0.
0
40
80
120
160
200
240
Pulse Height, PH, in picocoulombs

Figure 4

Figure 5

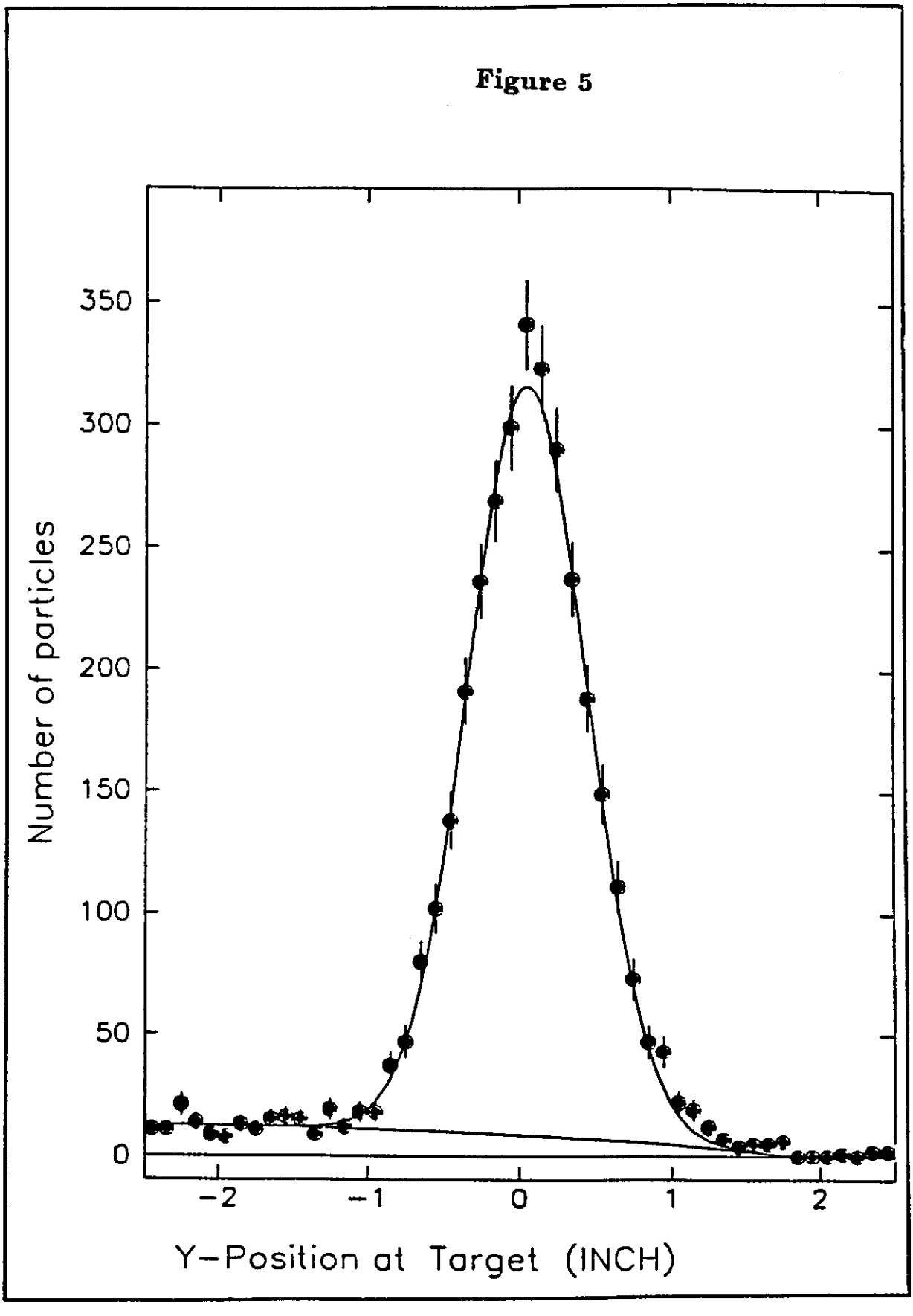
Number of particles
350
300
250
200
150
100
50
0
−2
−1
0
1
2
Y−Position at Target (INCH)

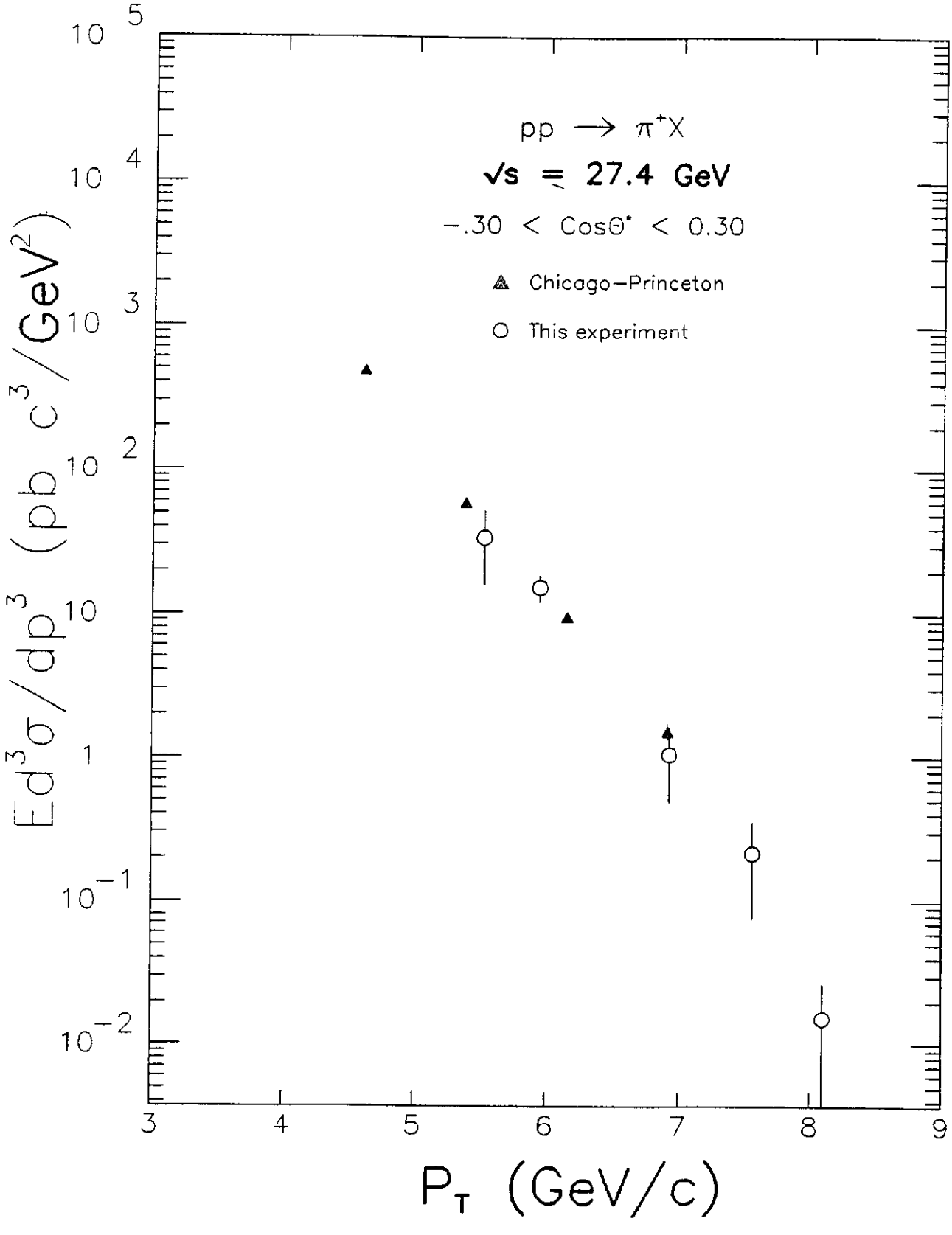
pp → π⁺X
√s = 27.4 GeV
−.30 < Cosθ* < 0.30
Chicago−Princeton
This experiment
Ed³σ/dp³ (pb c³/GeV²)
P_T (GeV/c)
10⁵
10⁴
10³
10²
10
1
10⁻¹
10⁻²
3
4
5
6
7
8
9

Figure 6a

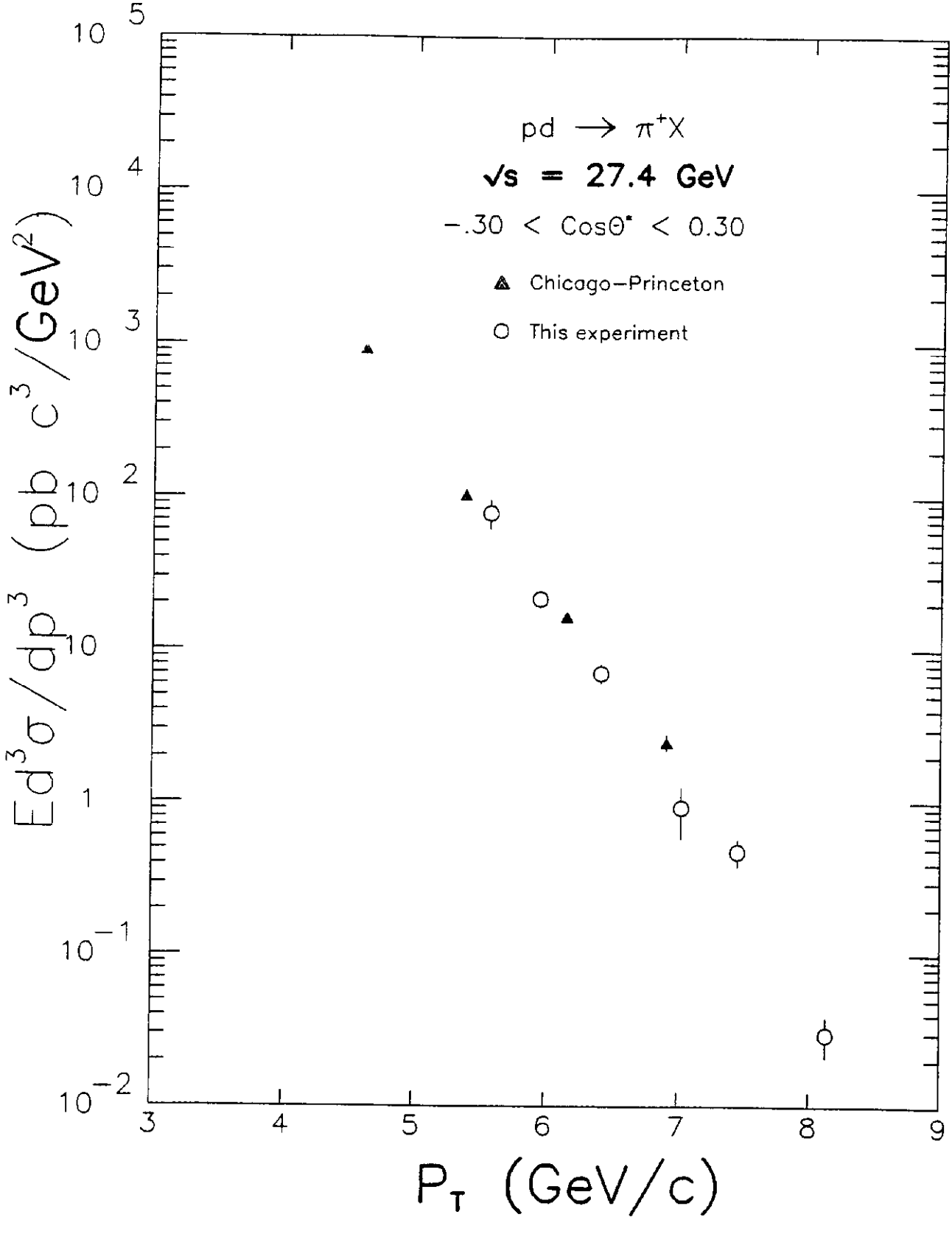
pd → π⁺X
√s = 27.4 GeV
−.30 < Cosθ* < 0.30
Chicago–Princeton
This experiment
Ed³σ/dp³ (pb c³/GeV²)
P_T (GeV/c)
10⁵
10⁴
10³
10²
10
1
10⁻¹
10⁻²
3
4
5
6
7
8
9

Figure 6b

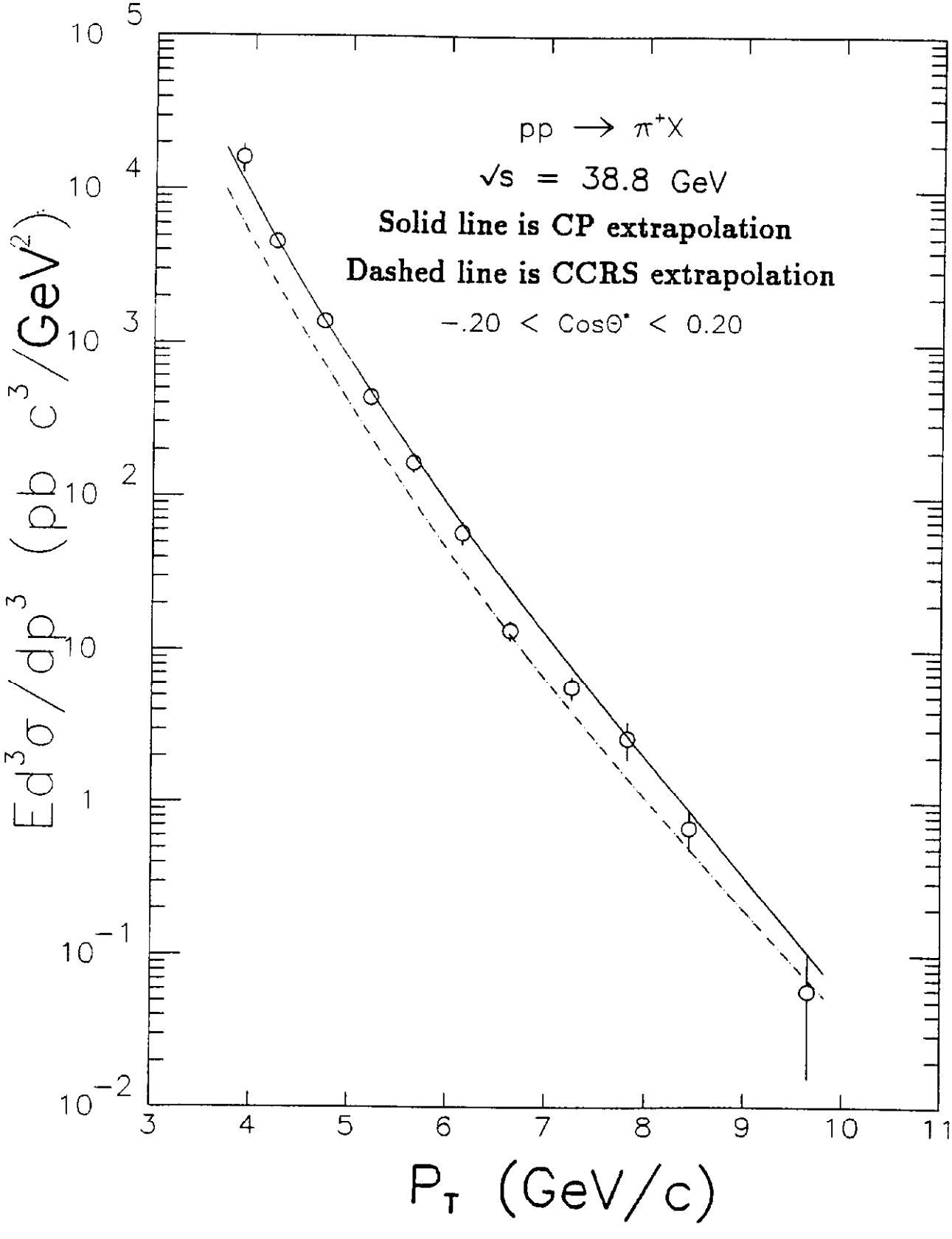
pp → π⁺X
√s = 38.8 GeV
Solid line is CP extrapolation
Dashed line is CCRS extrapolation
−.20 < Cosθ* < 0.20
Ed³σ/dp³ (pb c³/GeV²)
P_T (GeV/c)

Figure 6c

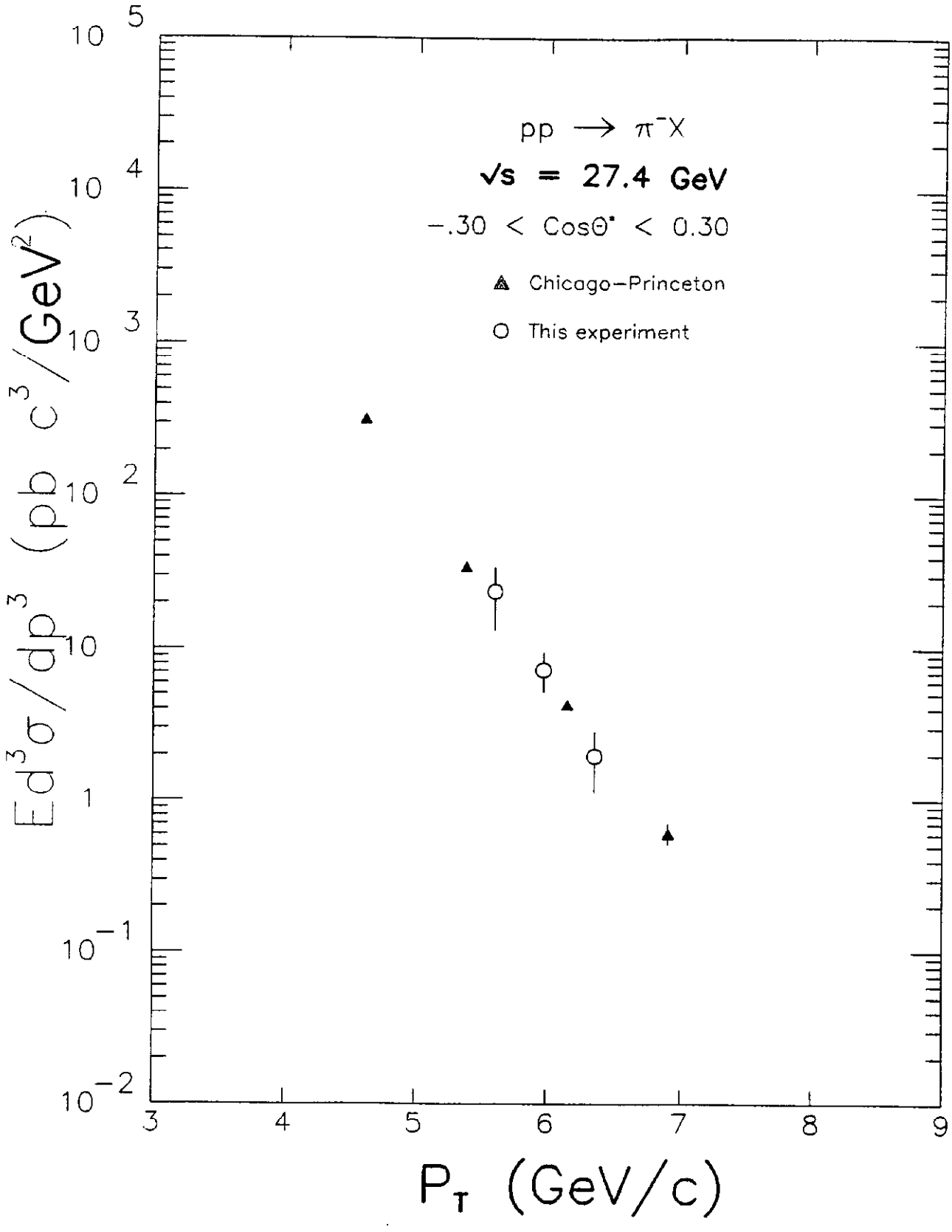
pp → π⁻X
√s = 27.4 GeV
−.30 < CosΘ* < 0.30
Chicago−Princeton
This experiment
Ed³σ/dp³ (pb c³/GeV²)
P_T (GeV/c)
10⁵
10⁴
10³
10²
10
1
10⁻¹
10⁻²
3
4
5
6
7
8
9

Figure 7a

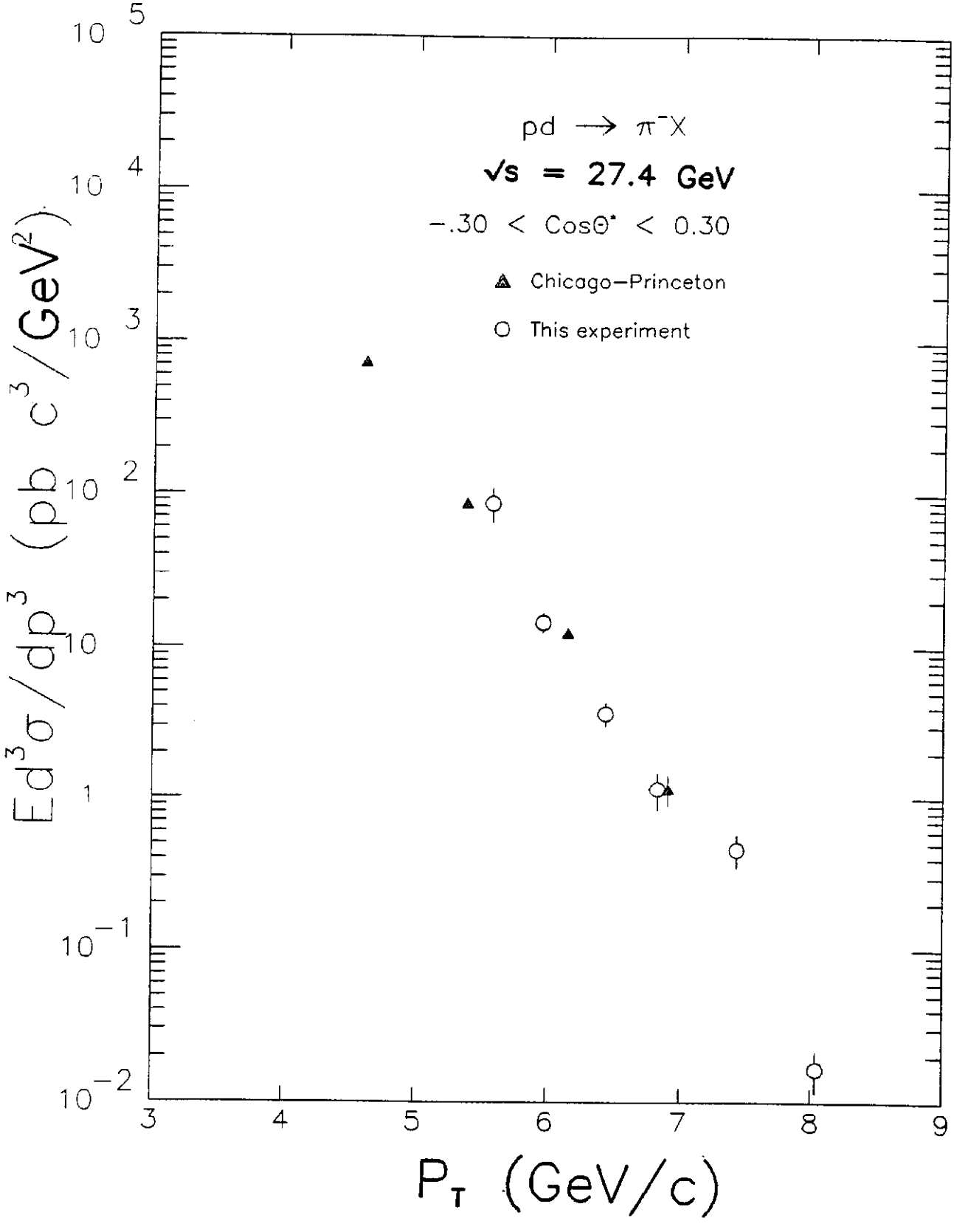
pd → π⁻X
√s = 27.4 GeV
−.30 < Cosθ* < 0.30
Chicago–Princeton
This experiment
Ed³σ/dp³ (pb c³/GeV²)
P_T (GeV/c)
10⁵
10⁴
10³
10²
10
1
10⁻¹
10⁻²
3
4
5
6
7
8
9

Figure 7b

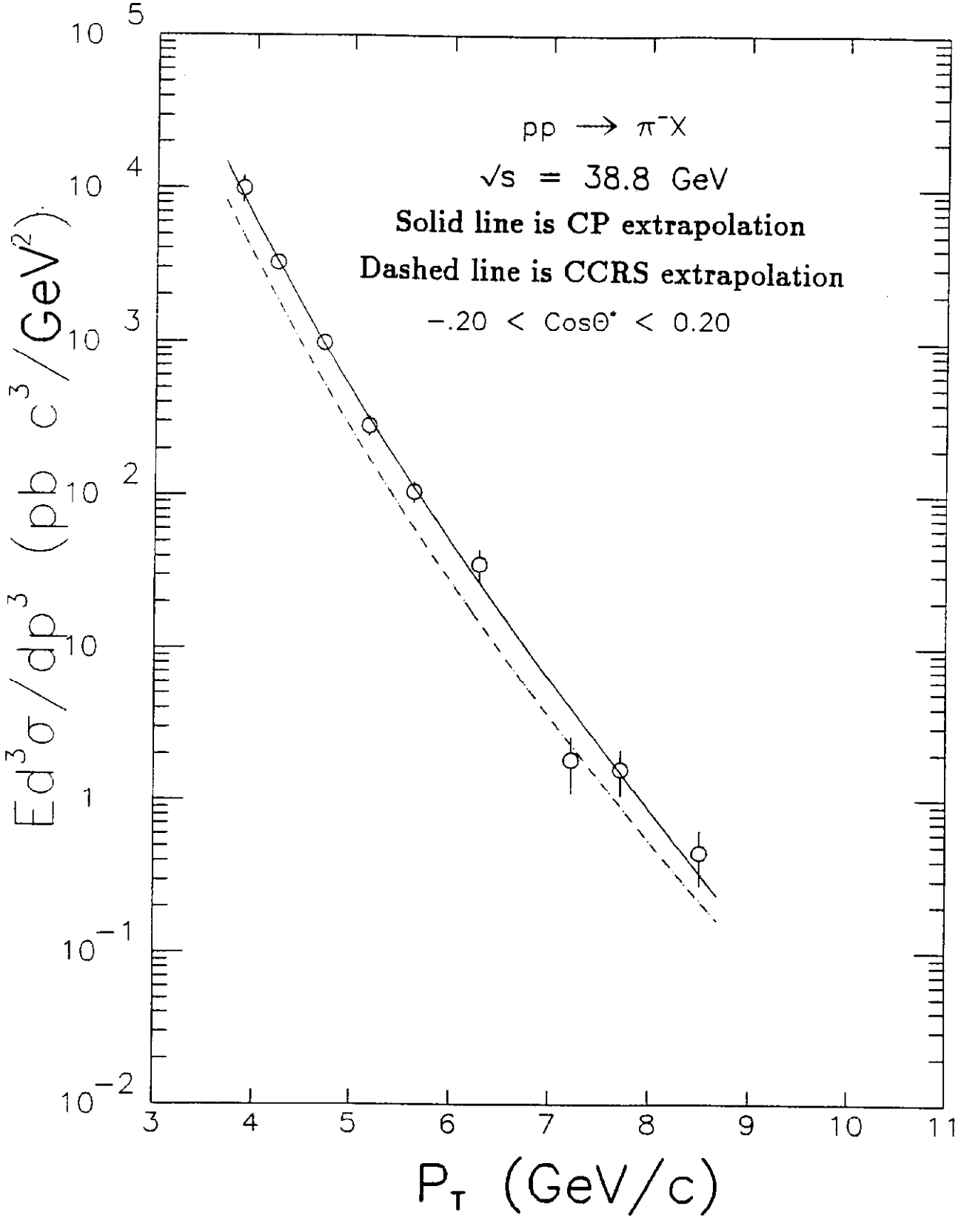
pp → π⁻X
√s = 38.8 GeV
Solid line is CP extrapolation
Dashed line is CCRS extrapolation
−.20 < CosΘ* < 0.20
Ed³σ/dp³ (pb c³/GeV²)
P_T (GeV/c)

Figure 7c

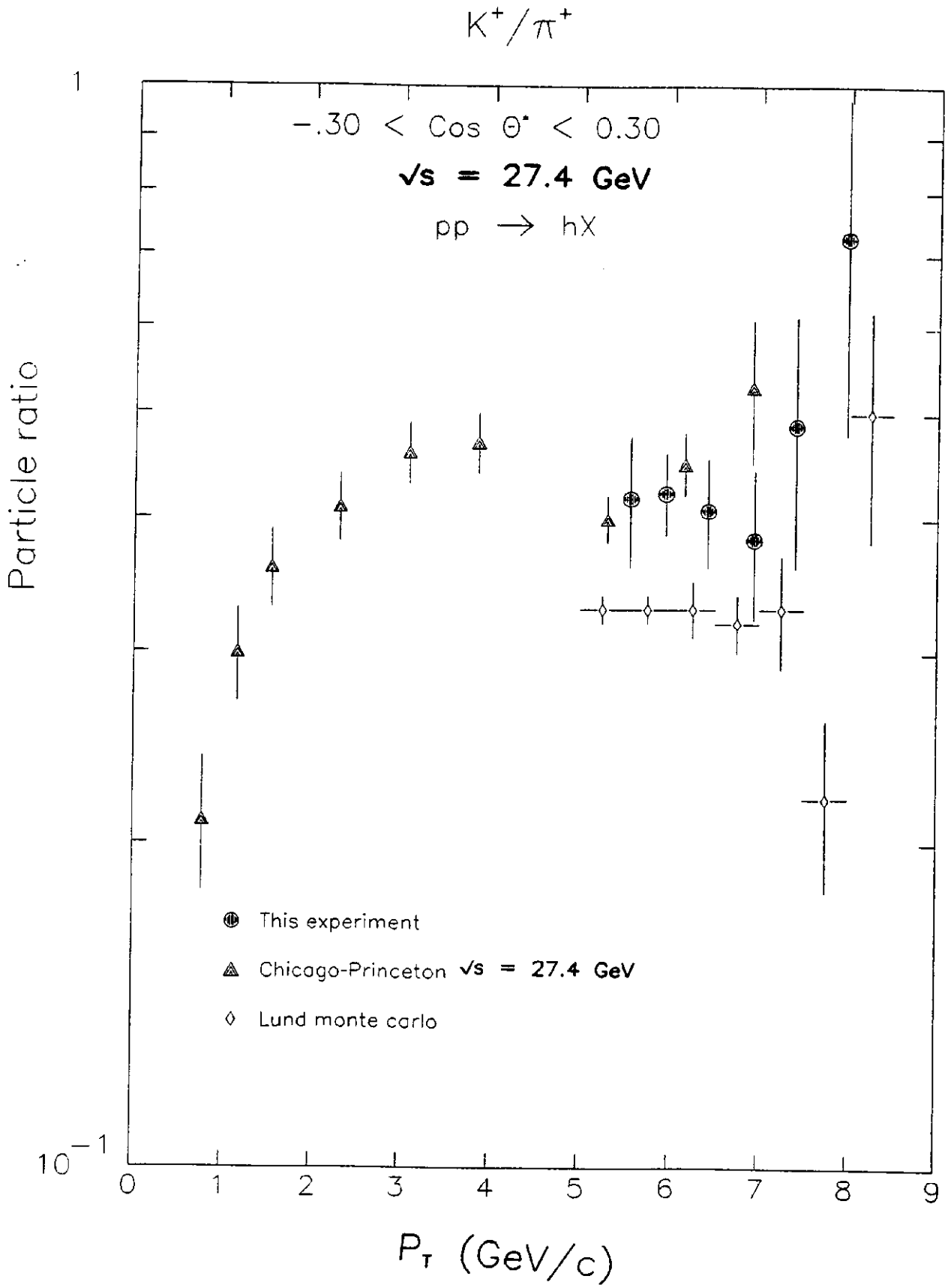
K^+/π^+
$-.30 < \cos\theta^* < 0.30$
$\sqrt{s} = 27.4$ GeV
$pp \rightarrow hX$
Particle ratio
1
10^{-1}
0
1
2
3
4
5
6
7
8
9
P_T (GeV/c)
This experiment
Chicago-Princeton $\sqrt{s} = 27.4$ GeV
Lund monte carlo

Figure 8a

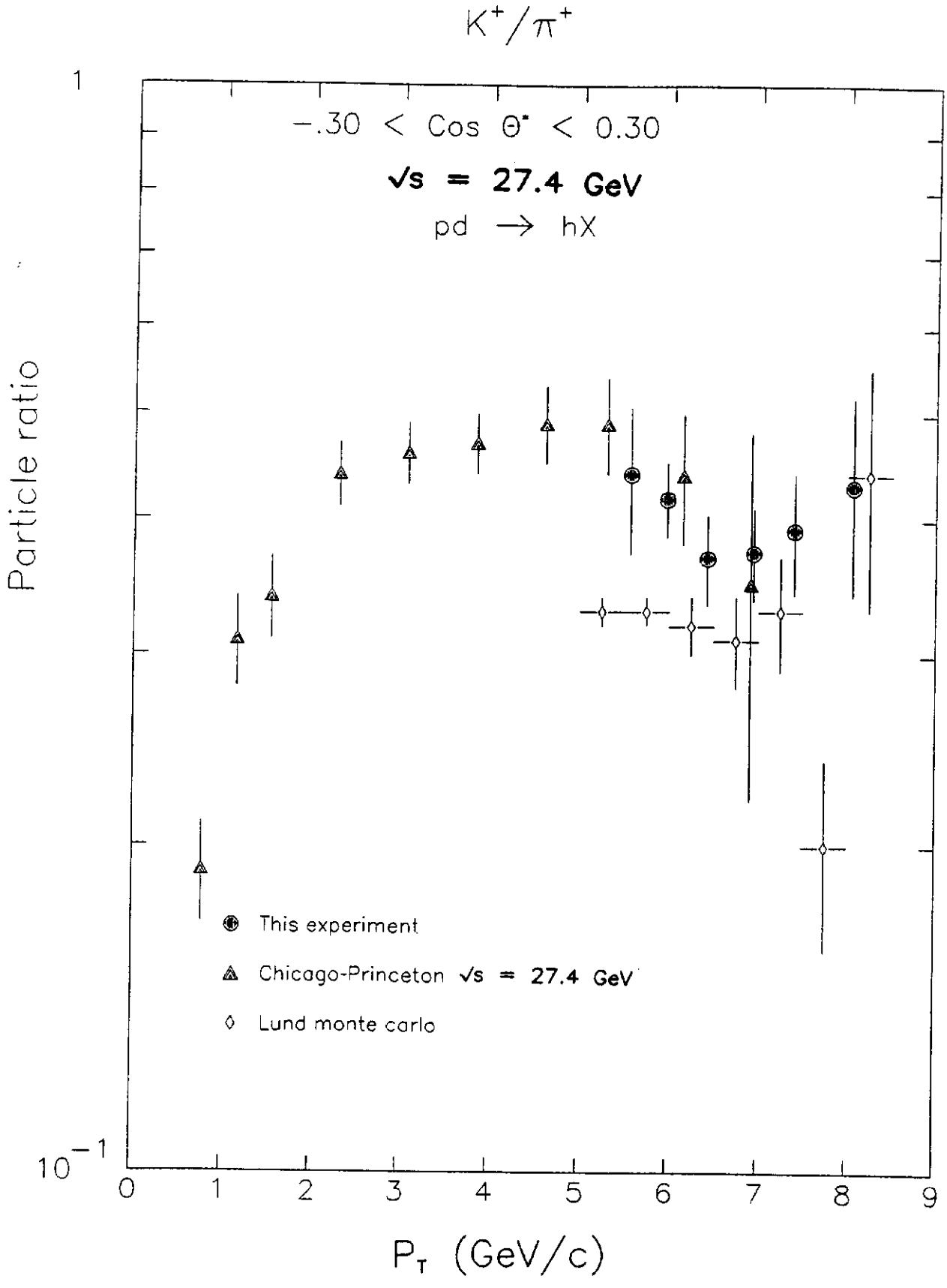
K^+/π^+
$-.30 < \cos\theta^* < 0.30$
$\sqrt{s}$ = 27.4 GeV
pd → hX
Particle ratio
This experiment
Chicago-Princeton $\sqrt{s}$ = 27.4 GeV
Lund monte carlo
P_T (GeV/c)

Figure 8b

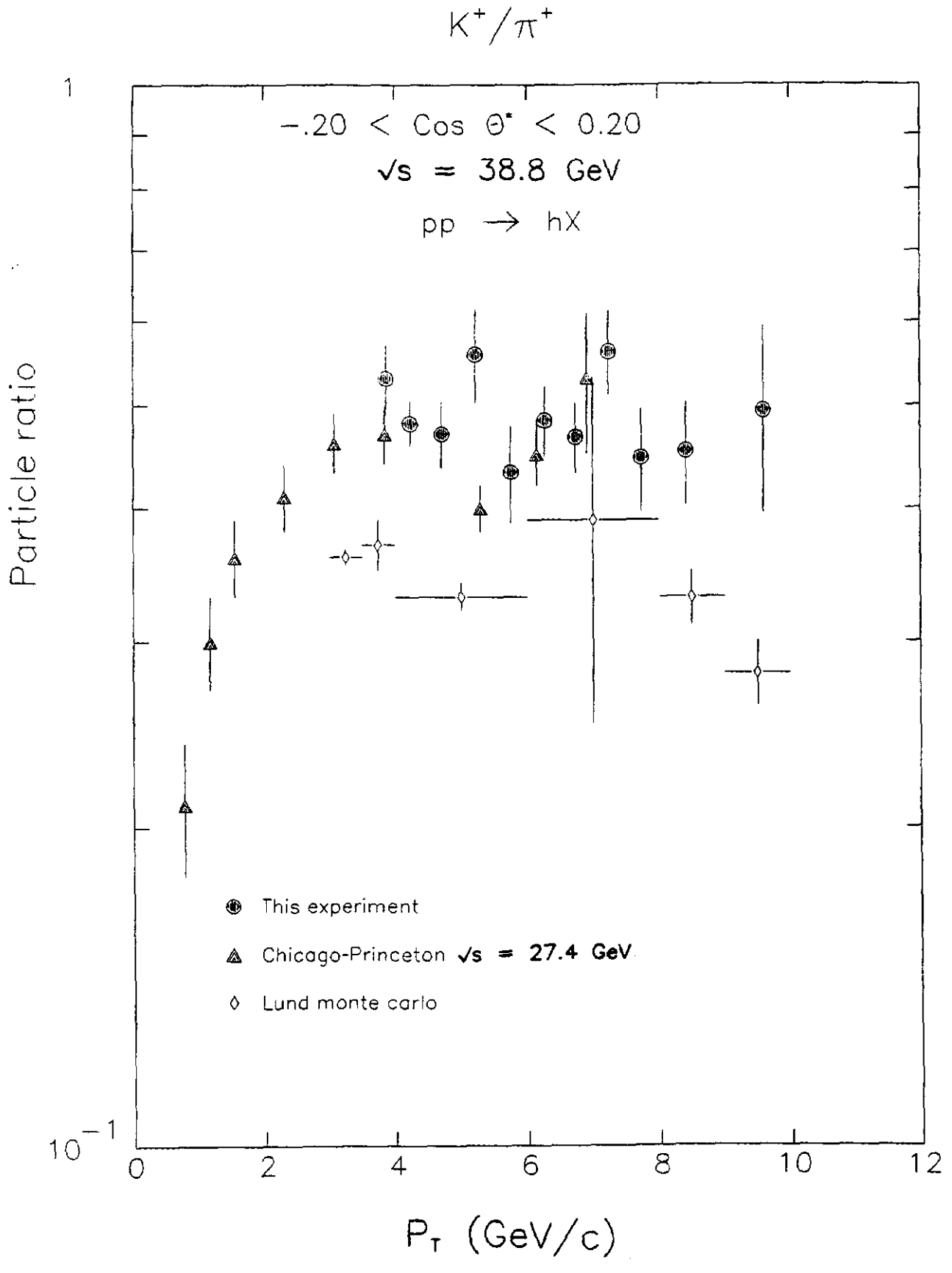
K^+/π^+
$-.20 < \cos\theta^* < 0.20$
$\sqrt{s} = 38.8$ GeV
$pp \rightarrow hX$
Particle ratio
1
10^{-1}
0
2
4
6
8
10
12
P_T (GeV/c)
This experiment
Chicago-Princeton $\sqrt{s} = 27.4$ GeV
Lund monte carlo

Figure 8c

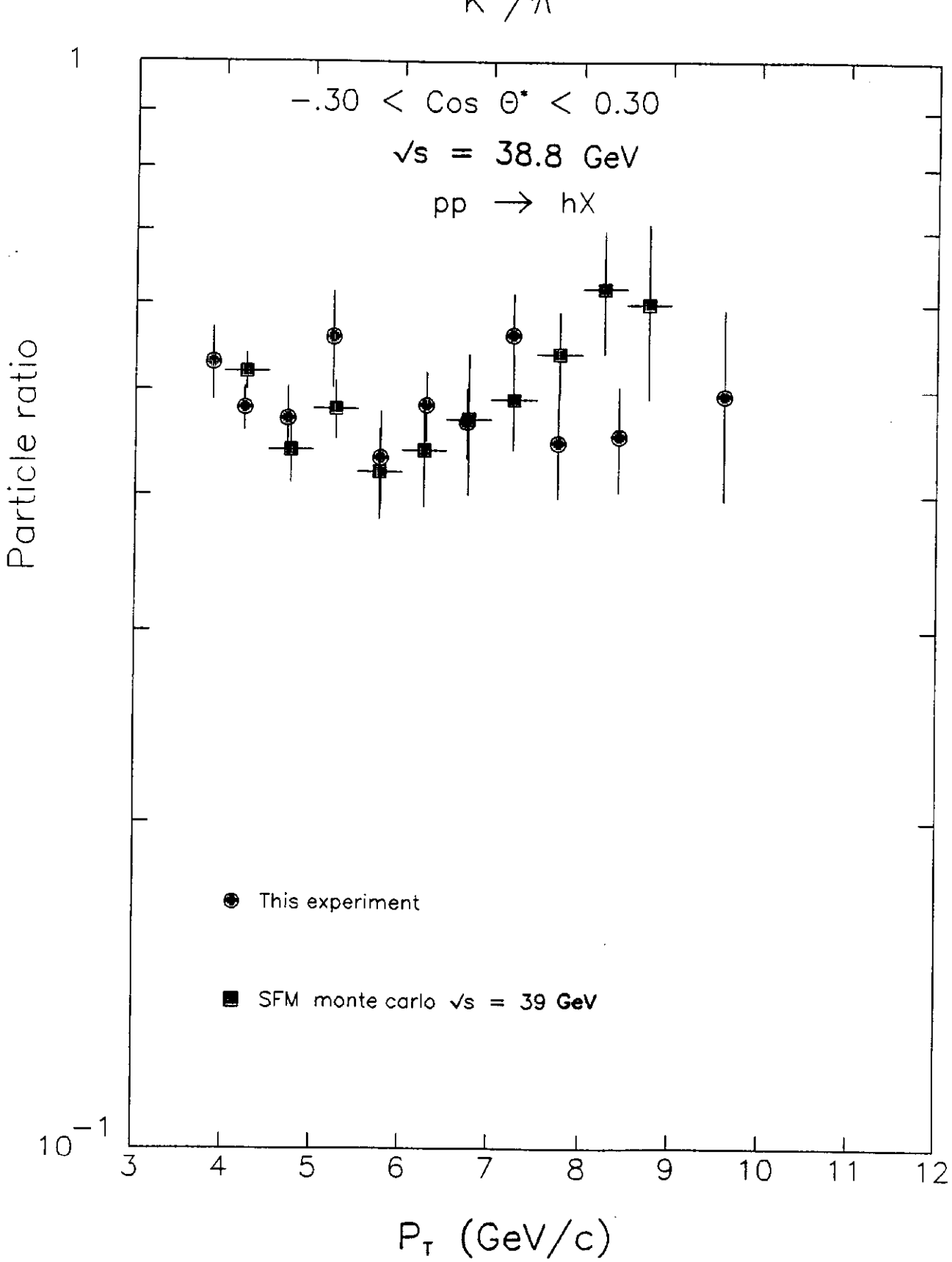
K^+/π^+
$-.30 < \text{Cos } \Theta^* < 0.30$
$\sqrt{s} = 38.8$ GeV
$pp \rightarrow hX$
Particle ratio
1
10^{-1}
This experiment
SFM monte carlo $\sqrt{s} = 39$ GeV
3
4
5
6
7
8
9
10
11
12
P_T (GeV/c)

Figure 8d

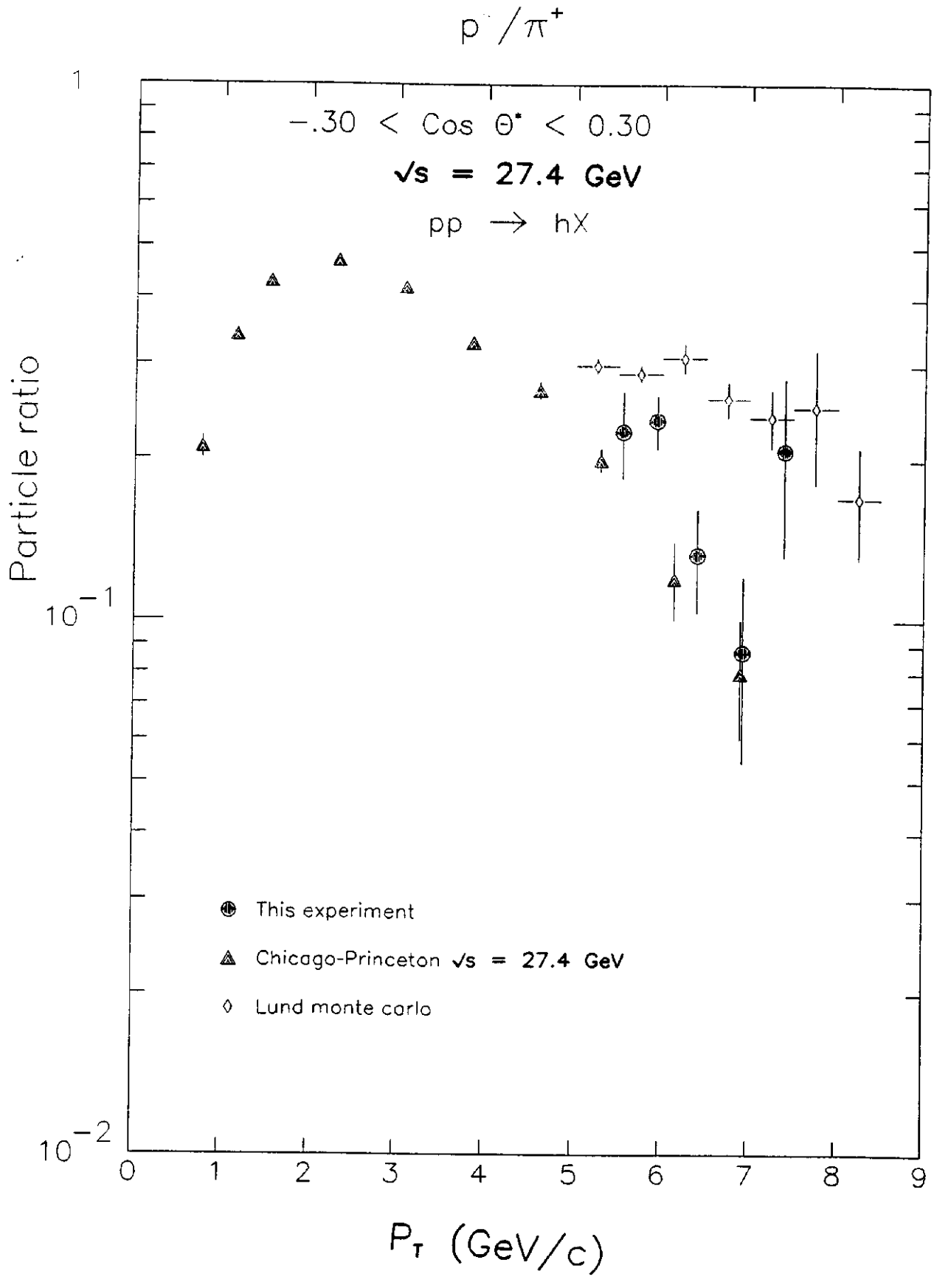
p̄ /π+
−.30 < Cos Θ* < 0.30
√s = 27.4 GeV
pp → hX
Particle ratio
1
10−1
10−2
0
1
2
3
4
5
6
7
8
9
This experiment
Chicago-Princeton √s = 27.4 GeV
Lund monte carlo
PT (GeV/c)

Figure 9a

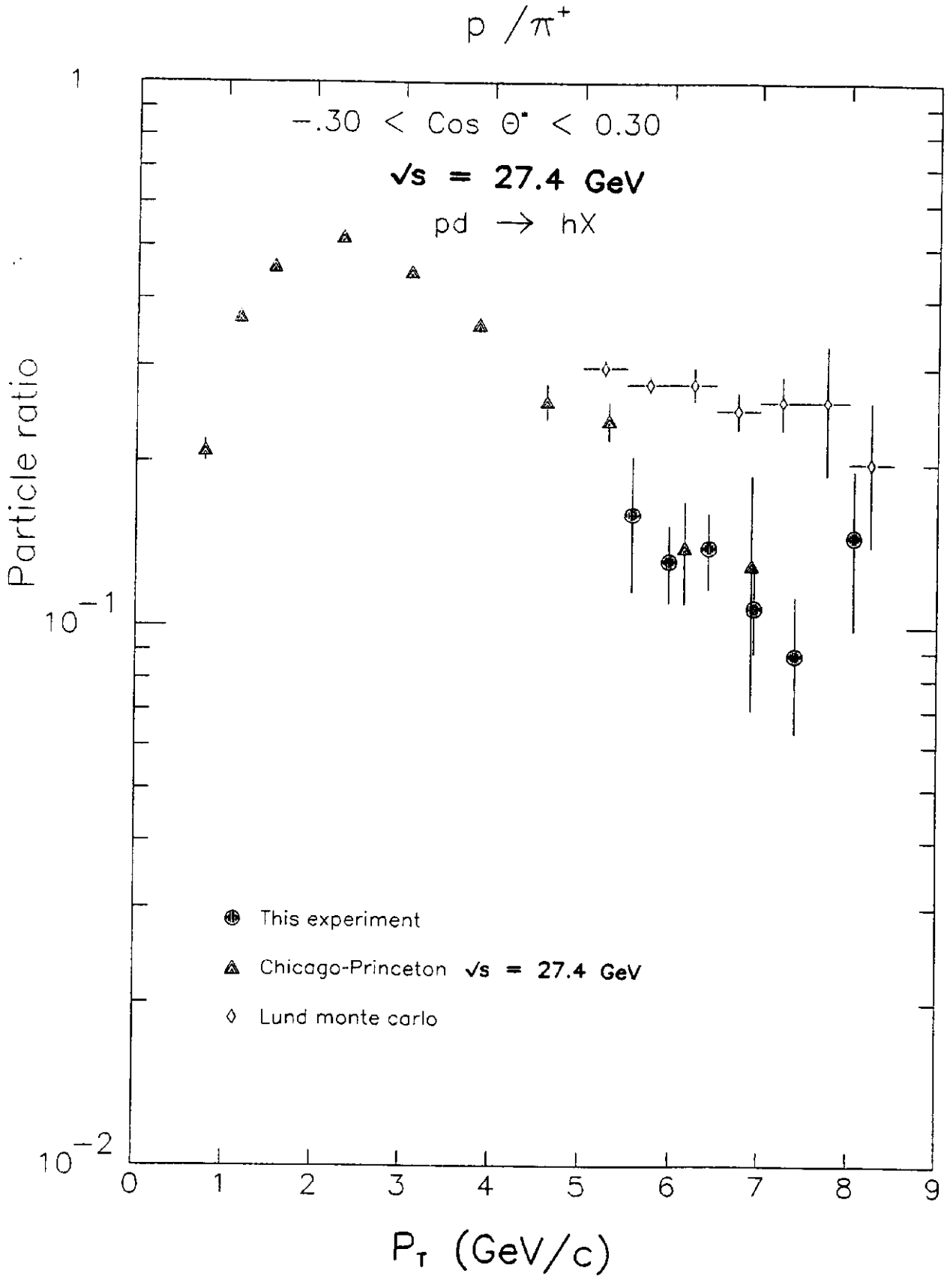
p /π+
−.30 < Cos θ* < 0.30
√s = 27.4 GeV
pd → hX
Particle ratio
1
10−1
10−2
0
1
2
3
4
5
6
7
8
9
PT (GeV/c)
This experiment
Chicago-Princeton √s = 27.4 GeV
Lund monte carlo

Figure 9b

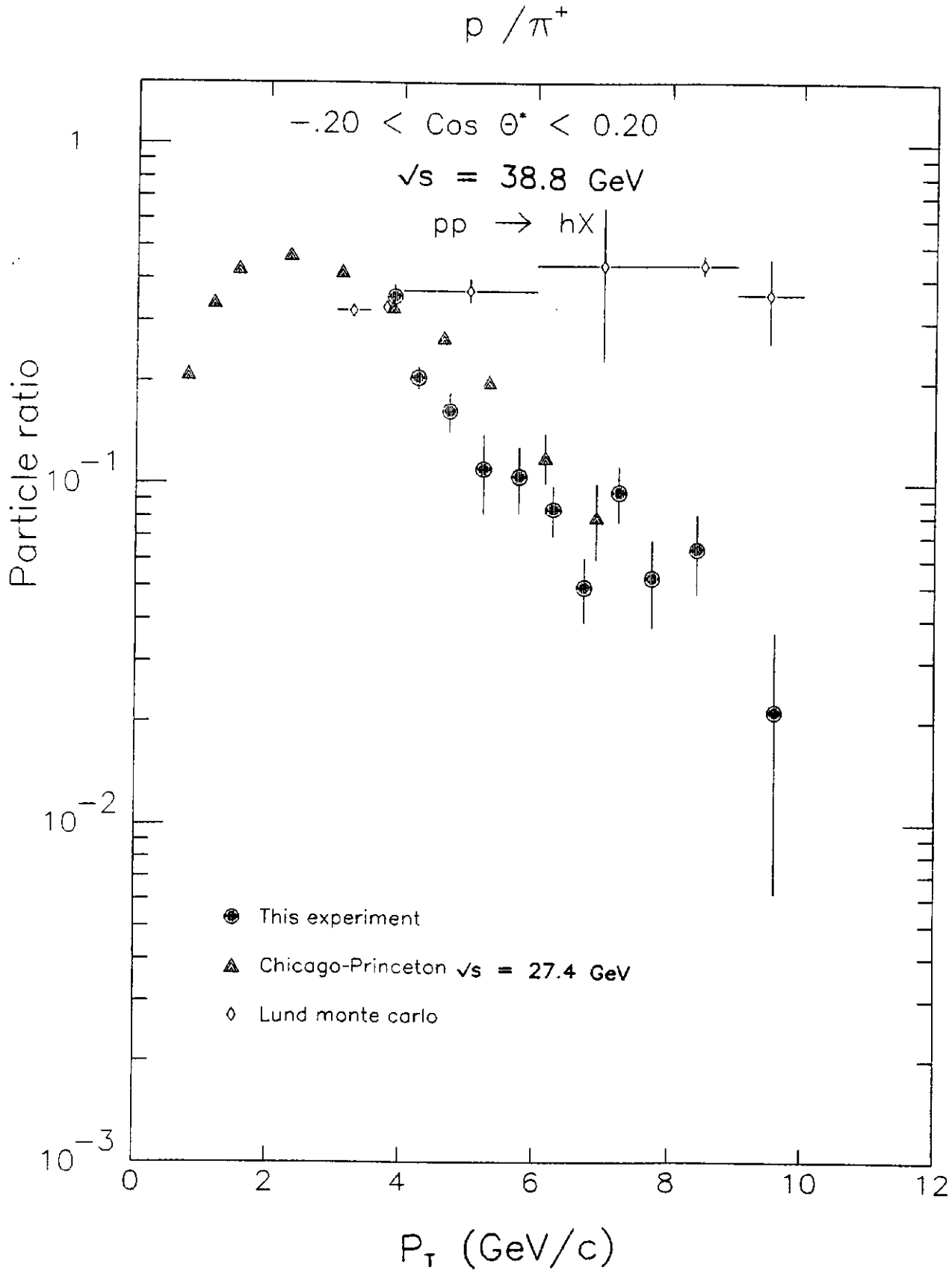
p /π+
−.20 < Cos Θ* < 0.20
√s = 38.8 GeV
pp → hX
Particle ratio
1
10−1
10−2
10−3
0
2
4
6
8
10
12
PT (GeV/c)
This experiment
Chicago-Princeton √s = 27.4 GeV
Lund monte carlo

Figure 9c

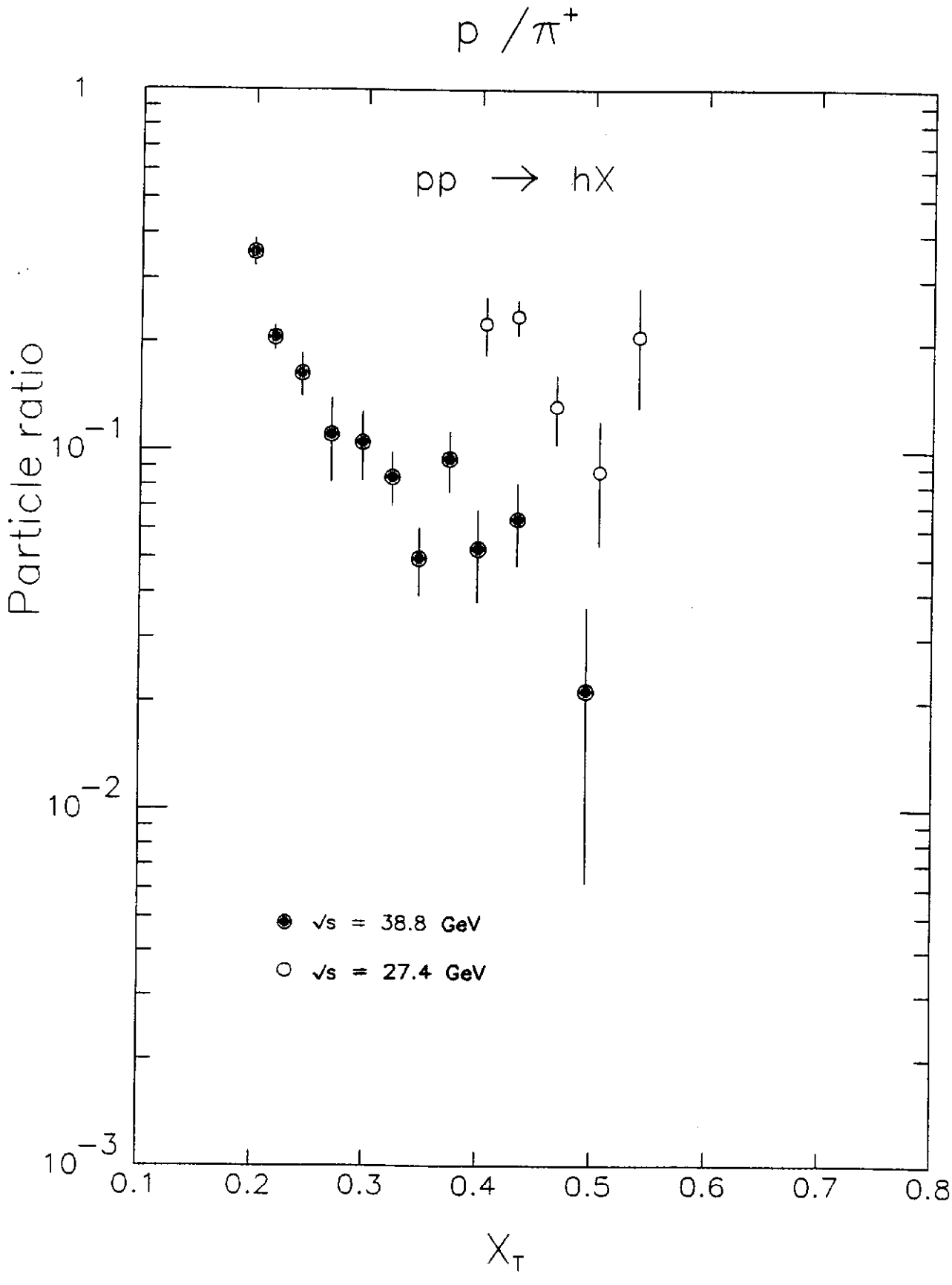
p /π+
pp → hX
Particle ratio
1
10−1
10−2
10−3
0.1
0.2
0.3
0.4
0.5
0.6
0.7
0.8
XT
√s = 38.8 GeV
√s = 27.4 GeV

Figure 10a

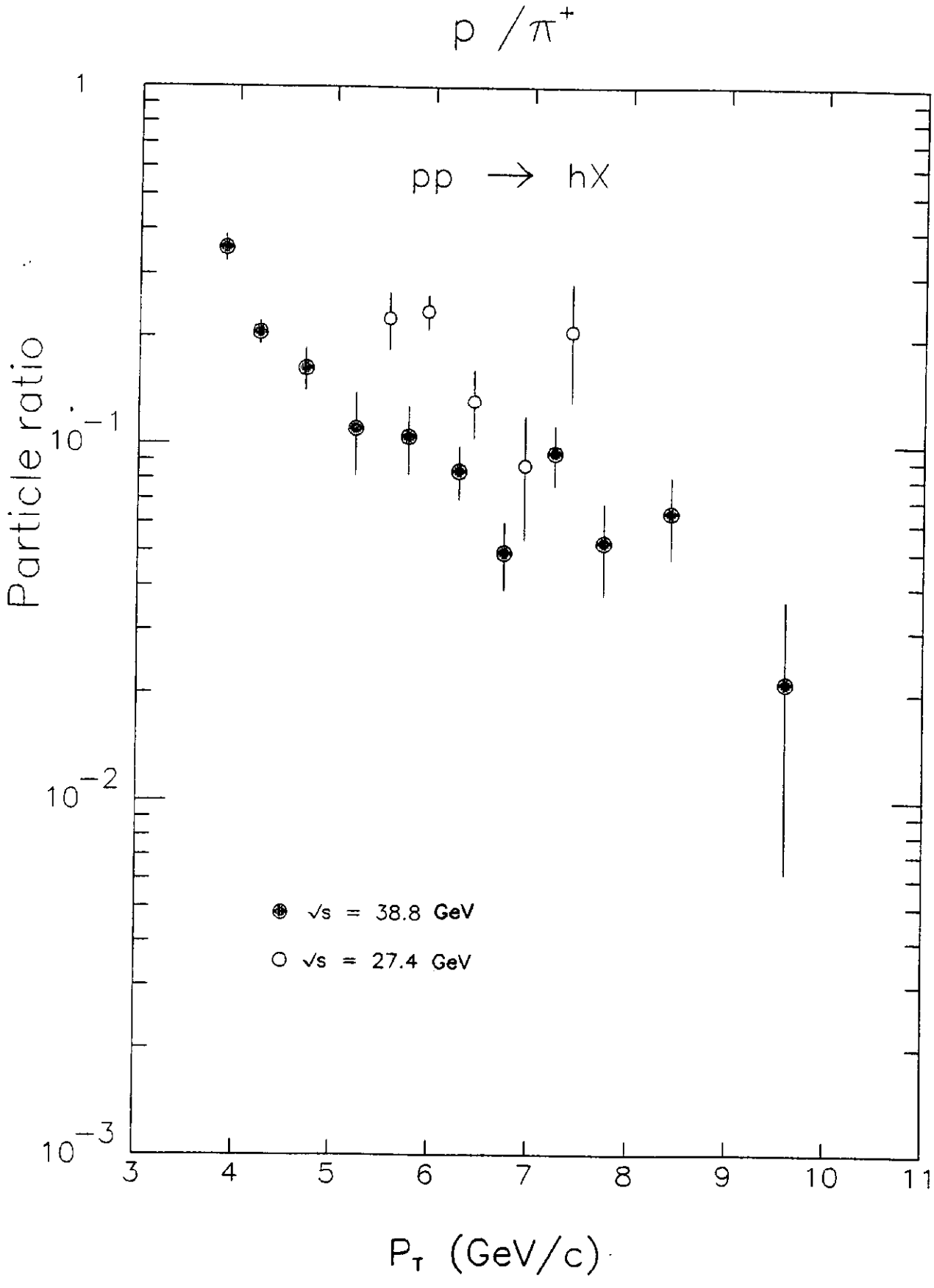
p /π+
pp → hX
Particle ratio
1
10−1
10−2
10−3
3
4
5
6
7
8
9
10
11
√s = 38.8 GeV
√s = 27.4 GeV
PT (GeV/c)

Figure 10b

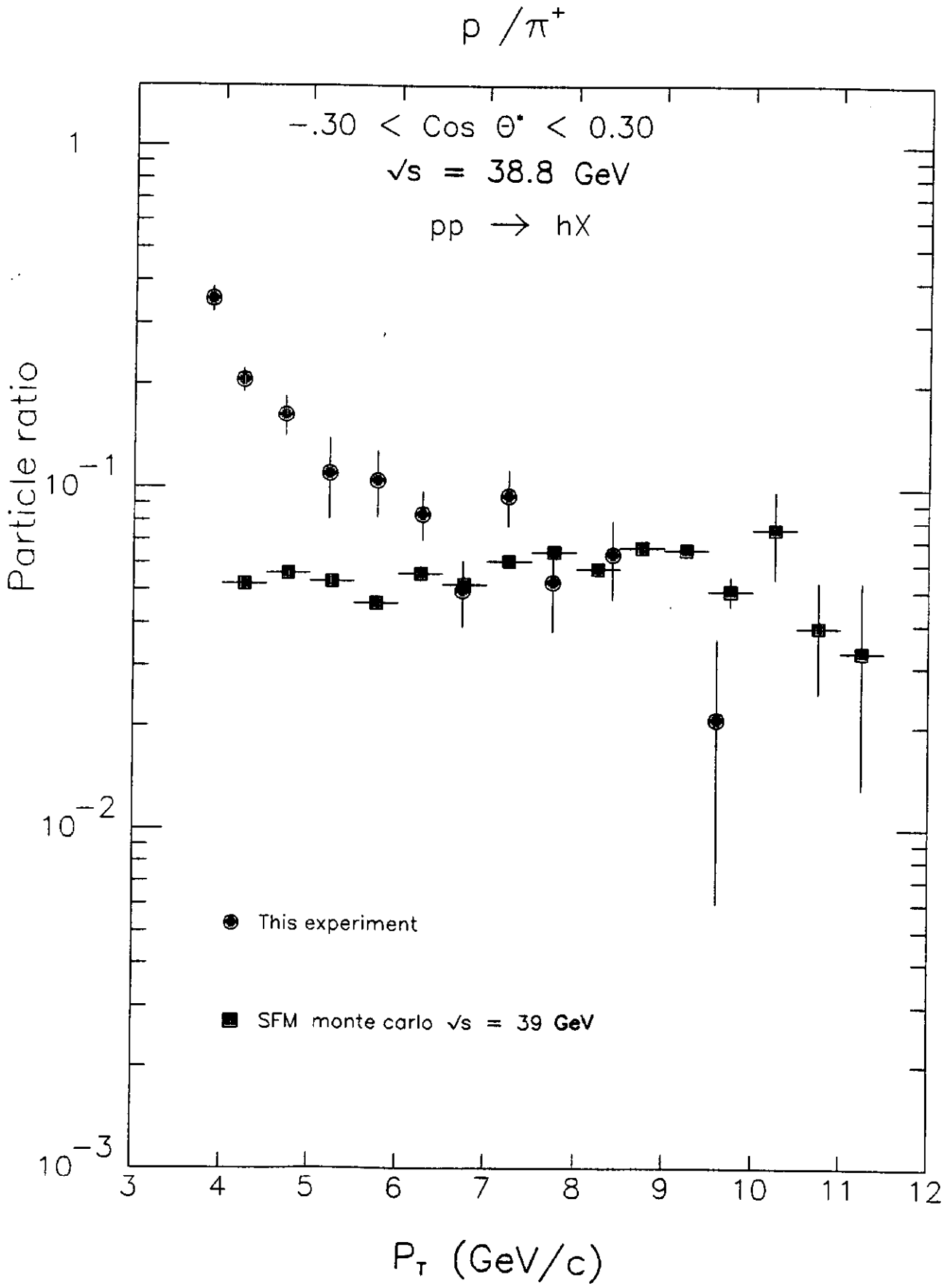
p /π+
−.30 < Cos Θ* < 0.30
√s = 38.8 GeV
pp → hX
Particle ratio
1
10−1
10−2
10−3
This experiment
SFM monte carlo √s = 39 GeV
3
4
5
6
7
8
9
10
11
12
PT (GeV/c)

Figure 10c

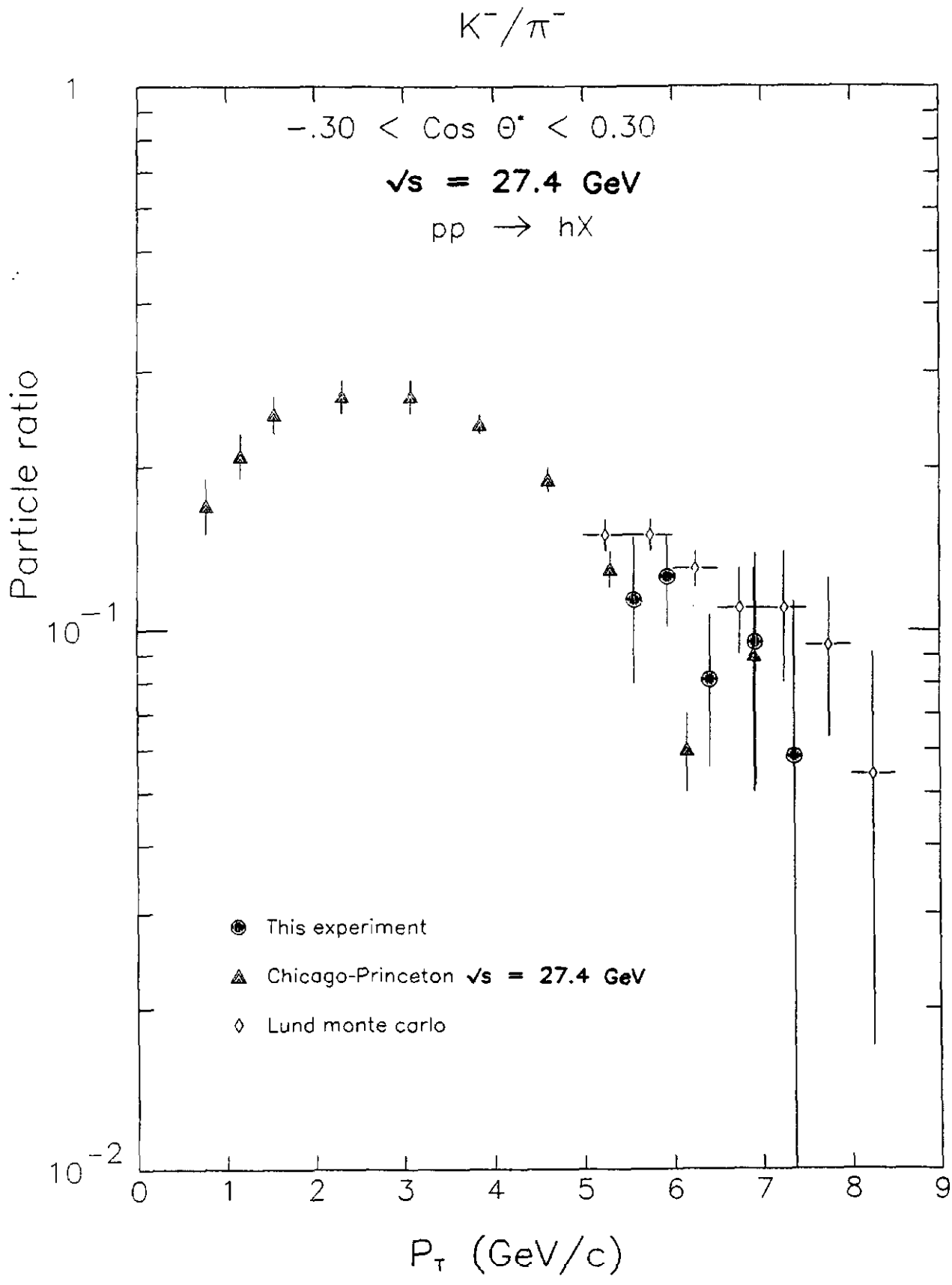
K^-/π^-
$-.30 < \cos\Theta^* < 0.30$
$\sqrt{s} = 27.4$ GeV
$pp \rightarrow hX$
Particle ratio
1
10^{-1}
10^{-2}
0
1
2
3
4
5
6
7
8
9
P_T (GeV/c)
This experiment
Chicago-Princeton $\sqrt{s} = 27.4$ GeV
Lund monte carlo

Figure 11a

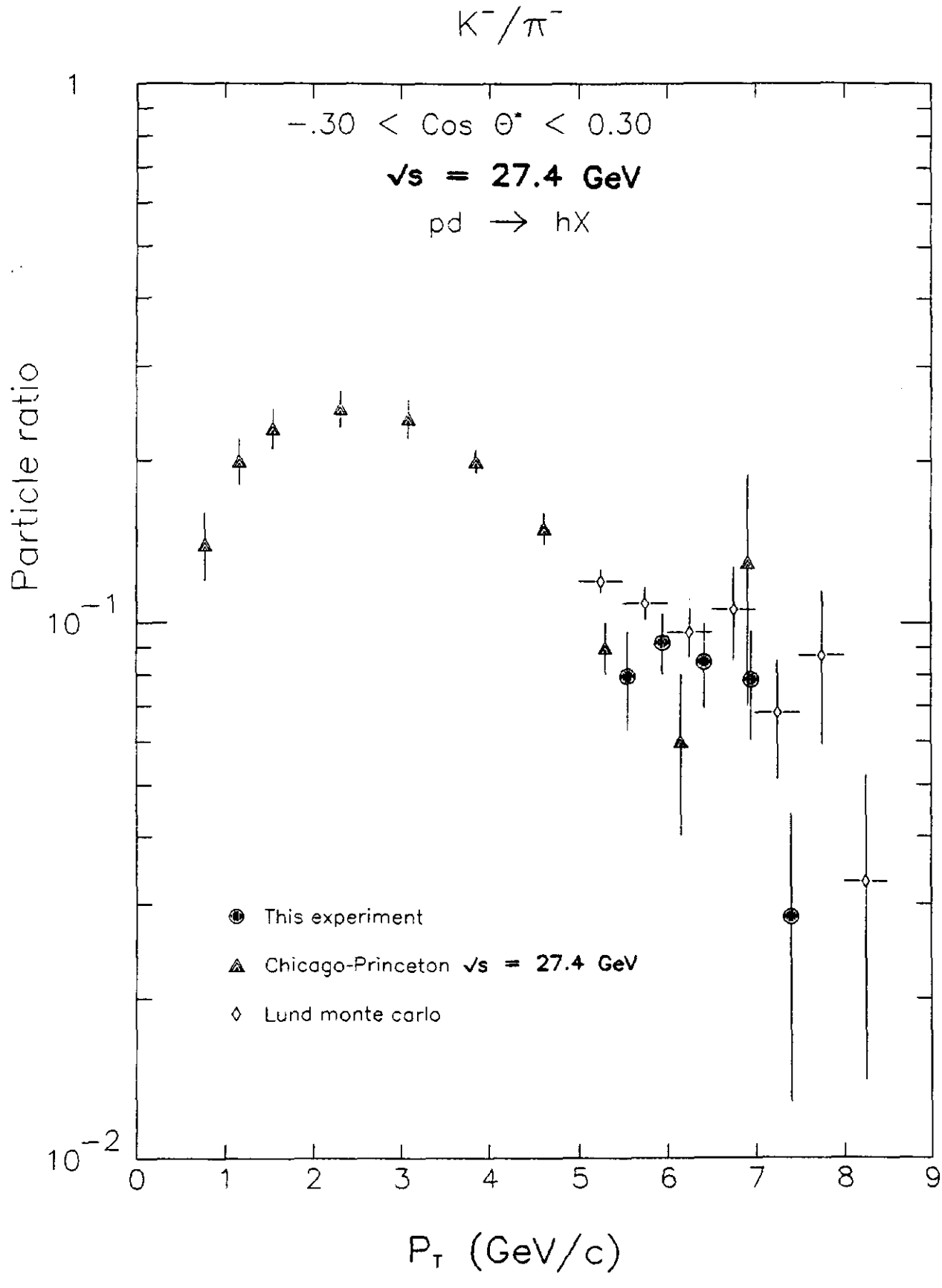
K^-/π^-
$-.30 < \cos\Theta^* < 0.30$
$\sqrt{s} = 27.4$ GeV
pd $\rightarrow$ hX
Particle ratio
1
10^{-1}
10^{-2}
0
1
2
3
4
5
6
7
8
9
P_T (GeV/c)
This experiment
Chicago-Princeton $\sqrt{s} = 27.4$ GeV
Lund monte carlo

Figure 11b

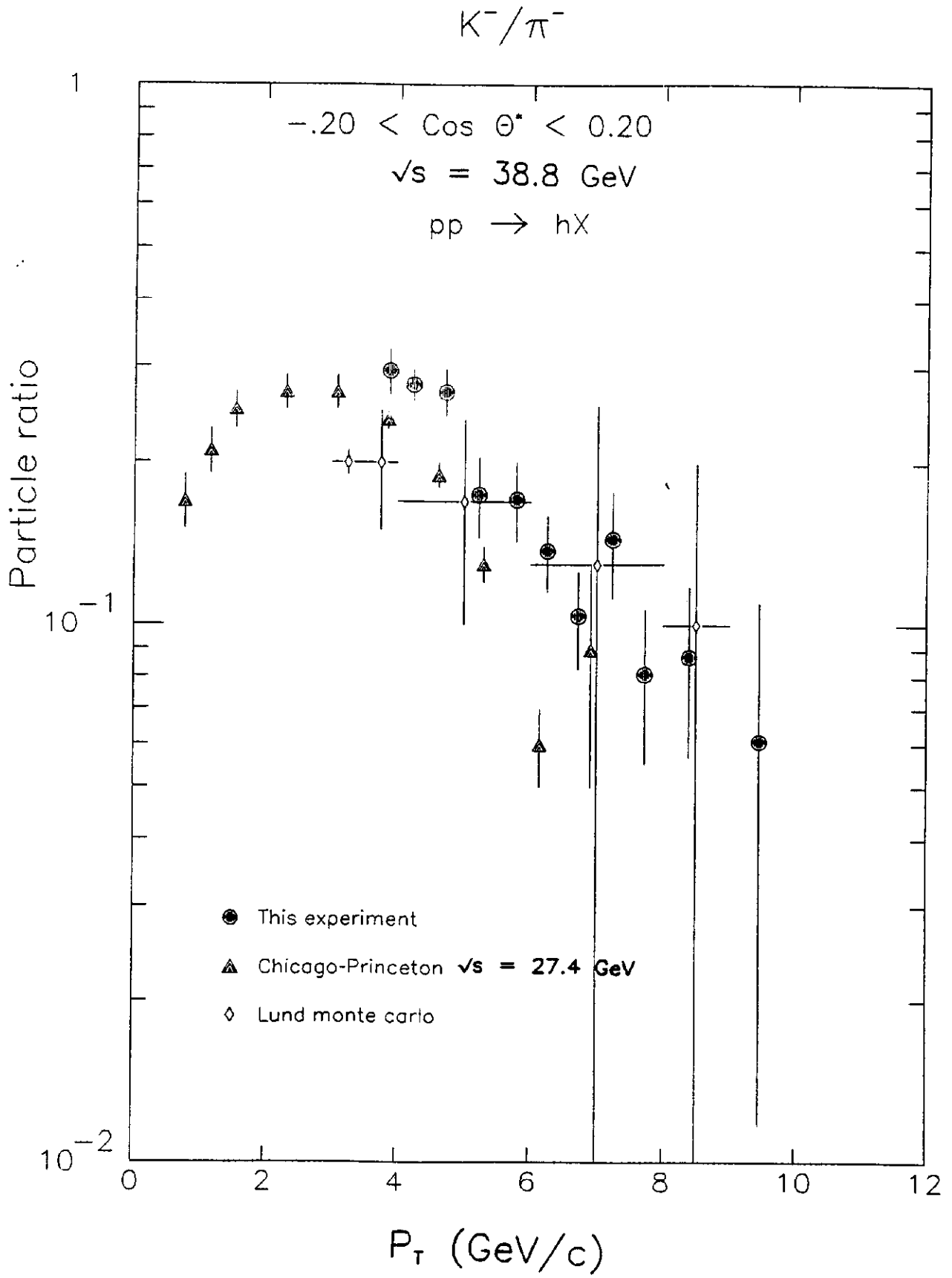
K^-/π^-
$-.20 < \cos\theta^* < 0.20$
$\sqrt{s} = 38.8$ GeV
$pp \rightarrow hX$
Particle ratio
1
10^{-1}
10^{-2}
0
2
4
6
8
10
12
P_T (GeV/c)
This experiment
Chicago-Princeton $\sqrt{s} = 27.4$ GeV
Lund monte carlo

Figure 11c

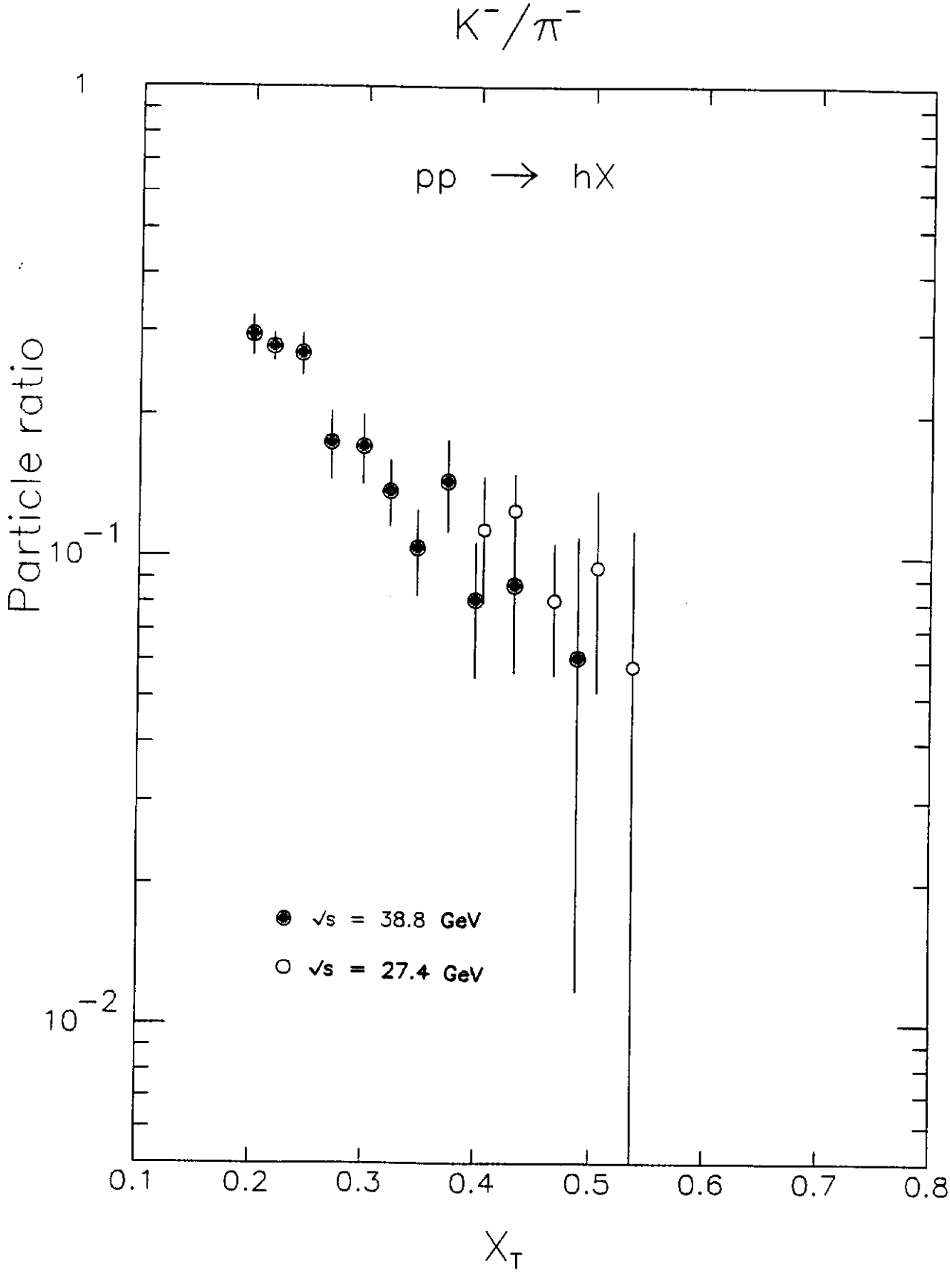
K^-/π^-
pp → hX
Particle ratio
1
10^{-1}
10^{-2}
√s = 38.8 GeV
√s = 27.4 GeV
0.1
0.2
0.3
0.4
0.5
0.6
0.7
0.8
X_T

Figure 12a

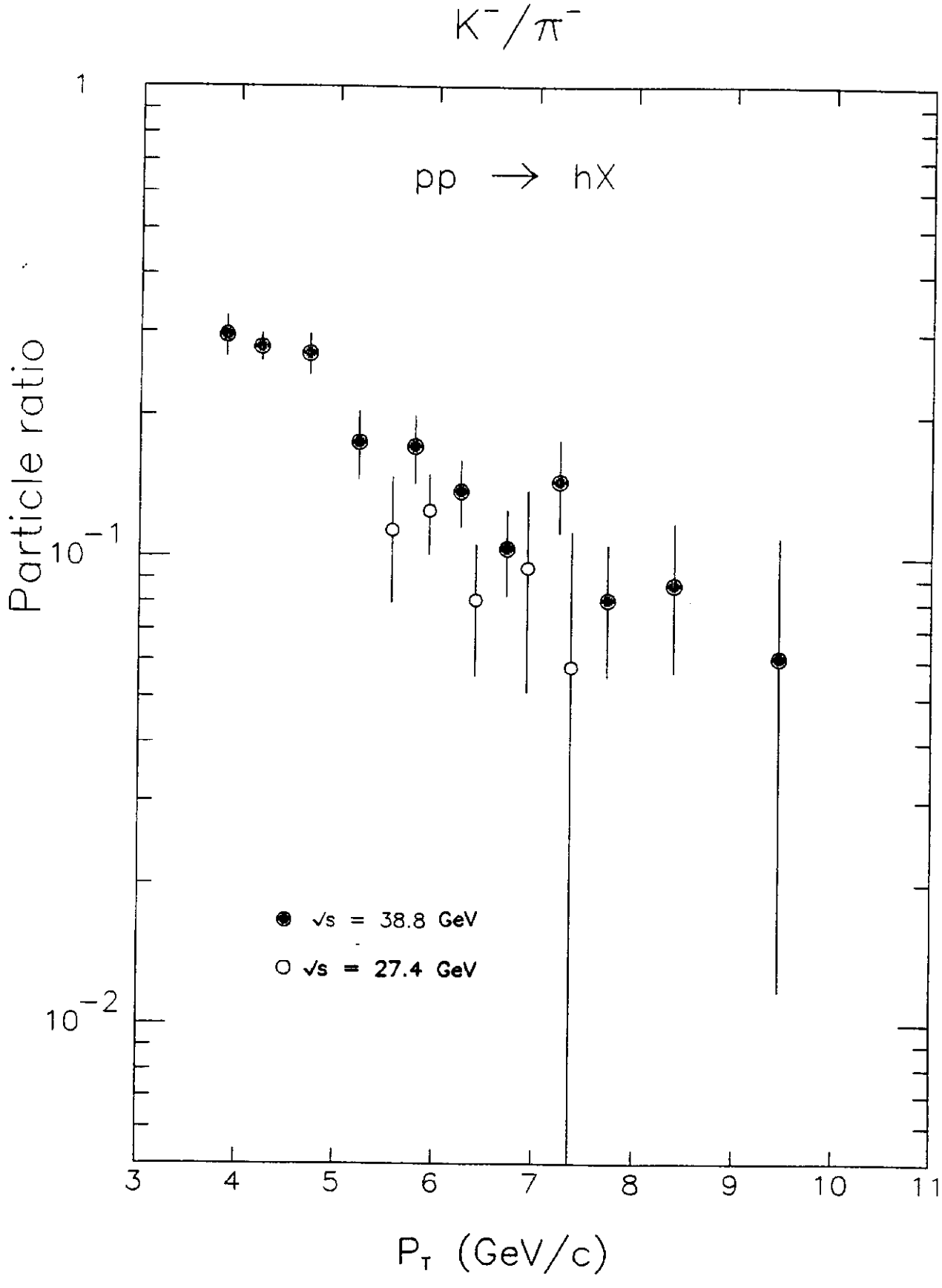
K^-/π^-
pp → hX
Particle ratio
1
10^{-1}
10^{-2}
√s = 38.8 GeV
√s = 27.4 GeV
3
4
5
6
7
8
9
10
11
P_T (GeV/c)

Figure 12b

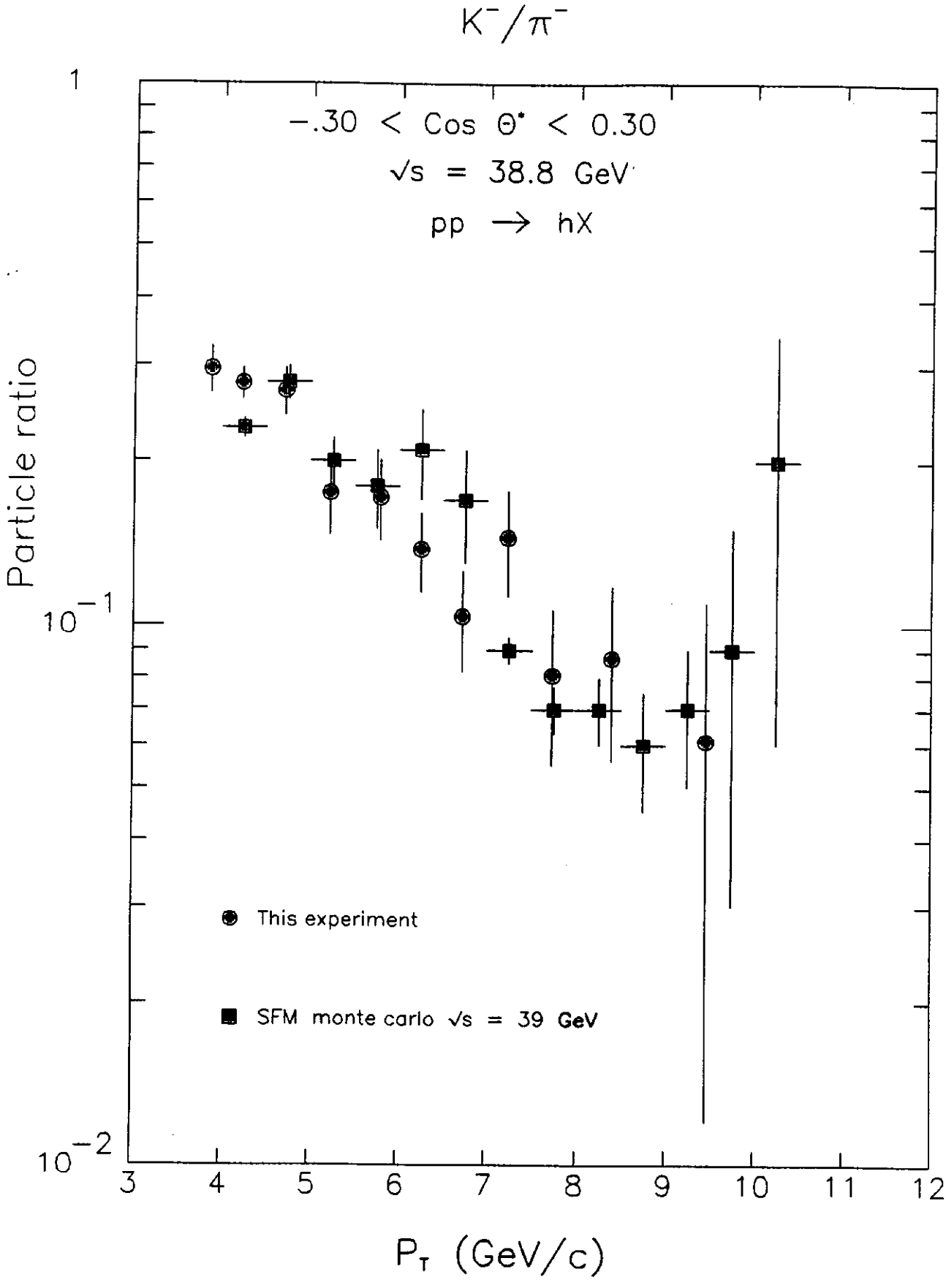
K^-/π^-
$-.30 < \cos\Theta^* < 0.30$
$\sqrt{s}$ = 38.8 GeV
pp → hX
Particle ratio
1
10^{-1}
10^{-2}
This experiment
SFM monte carlo $\sqrt{s}$ = 39 GeV
3
4
5
6
7
8
9
10
11
12
P_T (GeV/c)

Figure 12c